The Potential of Hue Angle Calculated Based on Multispectral Reflectance for Leaf Chlorophyll Content Estimation

Quanjun Jiao, Bing Zhang, *Fellow, IEEE*, Wenjiang Huang, Huichun Ye, Zhaoming Zhang, Binxiang Qian, Bohai Hu, and Shenglei Wang

***Abstract*— Remote sensing of leaf chlorophyll content (LCC) is critical in precision agriculture, forest monitoring, and pest management. Chlorophyll absorbs light in the visible and red-edge spectrum areas. However, many multispectral sensors lack red-edge bands. Subsequently, the development of effective visible chlorophyll-related indicators is important. The hue angle defined in the CIE xy chromaticity diagram, which reflects the human eye's color discrimination ability relying on visible light (400–700 nm), is introduced in this study for LCC estimation. This study proposes a new multispectral hue angle calculation method employing D65 standard illuminant data, investigates the effect of illuminant factors and band settings on hue angle calculation, and presents tristimulus weight coefficients for calculating MERIS, MSI, and ETM+ hue angles. Furthermore, the sensitivity of the link between LCC and different hue angles, as well as vegetation indices (VIs), is assessed in dense and sparse canopies. The results show that using wavelength-independent illuminant data or discrete bands overcalculates the reflectance-based hue angle. Moreover, our proposed hue angle calculated using D65 standard illuminant data is more sensitive to LCC than the existing hue angle using wavelength-independent illuminant data. In dense canopies, the multispectral hue angle has a stronger relationship with LCC than in sparse canopies. The multispectral hue angle generally appears weaker or similar to the red-edge VIs (MTCI and $CI_{red\text{-}edge}$), but stronger than the nonred-edge VIs (CI_{green}, NDVI, NGRDI, and TGI). These findings imply that the multispectral hue angle calculated from visible bands provides the potential to monitor the LCC of large-scale plants.**

***Index Terms*— Chlorophyll, color, hue angle, remote sensing, spectral indices, vegetation.**

Manuscript received 7 September 2022; revised 27 December 2022, 27 March 2023, 12 August 2023, and 12 September 2023; accepted 24 September 2023. Date of publication 4 October 2023; date of current version 17 October 2023. This work was supported in part by the National Natural Science Foundation of China under Grant 42030111 and Grant 42071330, and in part by the National Key Research and Development Program of China under Grant 2021YFB3900501. *(Corresponding author: Bing Zhang.)*

Quanjun Jiao, Huichun Ye, and Shenglei Wang are with the International Research Center of Big Data for Sustainable Development Goals, Beijing 100094, China, and also with the Key Laboratory of Digital Earth Science, Aerospace Information Research Institute, Chinese Academy of Sciences, Beijing 100094, China (e-mail: jiaoqj@radi.ac.cn; yehc@radi.ac.cn; wangsl@radi.ac.cn).

Bing Zhang and Wenjiang Huang are with the Key Laboratory of Digital Earth Science, Aerospace Information Research Institute, Chinese Academy of Sciences, Beijing 100094, China, and also with the College of Resources and Environment, University of Chinese Academy of Sciences, Beijing 100049, China (e-mail: zb@radi.ac.cn; huangwj@radi.ac.cn).

Zhaoming Zhang is with the China Remote Sensing Satellite Ground Station, Aerospace Information Research Institute, Chinese Academy of Sciences, Beijing 100094, China (e-mail: zhangzm@radi.ac.cn).

Binxiang Qian and Bohai Hu are with the Key Laboratory of Digital Earth Science, Aerospace Information Research Institute, Chinese Academy of Sciences, Beijing 100094, China, and also with the University of Chinese Academy of Sciences, Beijing 100049, China (e-mail: qianbinxiang20@mails.ucas.ac.cn; hubohai22@mails.ucas.ac.cn).

Digital Object Identifier 10.1109/TGRS.2023.3322130

I. Introduction

LEAF chlorophyll content (LCC) is a main proxy of vegetation photosynthetic potential, and its precise estimation is of great significance for monitoring of vegetation growth and health status [1], [2], [3]. Given that chlorophyll is the predominant pigment in most leaves, its optical absorption characteristics substantially influence the vegetation spectra [1], [2]. Chlorophyll forms blue and green peaks in the visible region (400–700 nm). Consequently, the reflectance of the leaf and canopy at blue and red wavelengths is lower than that at the green wavelength [4], [5]. Plant reflectance increases rapidly at the red-edge region (690–740 nm), due to a quick drop in chlorophyll absorption. The physical basis for remote sensing of the plant chlorophyll status is provided by a close relationship between vegetation reflectance and LCC [6], [7].

Vegetation indices (VIs) derived from spectral reflectance are frequently employed to monitor forest or crop LCC by ground, air, and satellite remote sensing platforms [6], [7], [8], [9]. Some VIs, based on red-edge wavelengths, have been found to be sensitive to vegetation chlorophyll status [10], [11], [12], [13]. Satellite sensors with red-edge spectral channels, such as the Medium Resolution Imaging Spectrometer (MERIS) on ENVIronmental SATellite (ENVISAT) and the MultiSpectral Instrument (MSI) on Sentinel-2, are used to produce red-edge chlorophyll-related VIs such as the MERIS terrestrial chlorophyll index (MTCI) [1], [10]. However, due to the cost, data storage, signal transmission, or signal-to-noise ratio constraints, satellite sensors, such as the Moderate Resolution Imaging Spectroradiometer (MODIS), the Enhanced Thematic Mapper Plus (ETM+), and some low-cost multispectral sensors onboard unmanned aerial vehicles (UAVs), lack red-edge narrow bands and only have visible and near-infrared (NIR) bands or even only visible bands. Despite this limitation, various studies have attempted to overcome these challenges by utilizing the visible and NIR bands to design chlorophyll-related VIs, such as the green chlorophyll index (CI_{green}) [1], [14], [15]. However, the accuracy of LCC estimation using these indices is not satisfactory, particularly when

1558-0644 © 2023 IEEE. Personal use is permitted, but republication/redistribution requires IEEE permission.
See https://www.ieee.org/publications/rights/index.html for more information.

Authorized licensed use limited to: Aerospace Information Research Institute. Downloaded on October 19,2023 at 00:37:32 UTC from IEEE Xplore. Restrictions apply.

TABLE I
STATISTICAL INFORMATION OF GROUND-MEASURED VEGETATION PARAMETERS CORRESPONDING TO CANOPY- AND SATELLITE-LEVEL REFLECTANCE MEASUREMENTS

Data sets	Sites	Spectral measurement	Sampling periods	n	LCC ($\mu g\ cm^{-2}$)				LAI ($m^2\ m^{-2}$)			
					Mean	SD	Min	Max	Mean	SD	Min	Max
Soybean-Hyper	US-Ne2 & US-Ne3	Canopy-level hyperspectral	June–September in 2002 and 2004	73	33.59	10.28	12.06	64.88	2.59	1.42	0.16	5.45
Soybean-MERIS	US-Ne2	Satellite-level multispectral	June–September in 2004	21	37.92	14.47	12.06	64.88	2.81	1.33	0.20	4.32
Soybean-ETM+	US-Ne2 & US-Ne3	Satellite-level multispectral	June–September in 2002 and 2004	13	35.93	7.93	26.44	51.93	2.65	1.55	0.39	4.94
Wheat-MSI	Beijing-Shunyi	Satellite-level multispectral	April–May in 2016	92	60.16	16.74	16.87	101.23	4.23	1.81	0.96	8.16

calculated using canopy reflectance rather than leaf reflectance [16], [17]. To accurately map the vegetation chlorophyll status and analyze its long-term trend, it is very meaningful to better explore chlorophyll-related remote sensing indicators for commonly used multispectral sensors without the red-edge bands.

The natural world's colors are perceived by the human eye, camera, and other remote sensors. The color difference aids in distinguishing the types and attributes of objects, and the human eye frequently distinguishes green vegetables with differing chlorophyll content via color. To continuously represent the changing colors recognized by the human eye, the International Commission on Illumination (CIE) developed the CIE XYZ color space in which tristimulus values (X, Y, and Z) can be transformed from an object's reflectivity, utilizing the CIE XYZ color matching functions and standard illuminant data [18]. The CIE reduced the 3-D color space even further to the CIE *xy* chromaticity diagram, where x and y are independent of the luminance Y [18]. The specific x and y are transformed into a 1-D hue angle as a new color indicator based on visible reflectance data by using the white point as a new origin point in the CIE xy chromaticity diagram [19], [20], [21]. The x and y two-dimensional information has been used to monitor water, vegetation, and other ground features [22], [23], [24]. In comparison to the (x, y) color representation, it has been recently deduced that the hue angle is easily utilized for water color monitoring [25], [26], [27], [28]. However, the application of vegetation remote sensing based on reflectance-based hue angle is rarely reported. In addition, the tristimulus values in these water studies were derived from the integration of water remote sensing reflectance without the use of any illuminant data, that is, the existing calculation of the water multispectral hue angle employs a special case of illuminant data whose intensity does not change with wavelength (called wavelength-independent illuminant data), which is incompatible with the CIE XYZ color space's standard illuminant condition. This may reduce the sensitivity of the existing multispectral hue angle to LCC. The evaluation of the performance of vegetation chlorophyll estimation with reflectance-based hue angle calculated based on remote sensing data, defined in the CIE xy chromaticity diagram, needs to be further improved. Furthermore, the band number factor of the multispectral sensor must be considered when calculating the vegetation hue angle [21], [28]. Given the poor accuracy in VI-based estimating chlorophyll content in sparse canopies with low leaf area index (LAI) [7], [15], determining the applicability of a new multispectral hue angle for different canopies is also required.

Therefore, the objective of this study is to develop a new multispectral hue angle calculation method from visible bands employing D65 standard illuminant data, investigate the impact of the illuminant data selections and band settings on reflectance-based hue angle calculation, and determine the potential of estimating LCC using our proposed multispectral hue angle through correlation analysis, particularly for the canopy- and satellite-level nonred-edge sensors. To represent different band configurations, hyperspectral data and three multispectral data—MERIS, MSI, and ETM+—are used. Furthermore, the LCC estimation performance of the reflectance-based hue angles is compared with that of the popular red-edge, visible–NIR, and visible VIs.

II. DATA

To test reflectance-based hue angle calculation algorithms and the sensitivity between the hue angle and LCC in $\mu g\ cm^{-2}$, ground-measured canopy-level hyperspectral data, simulated multispectral data generated from the hyperspectral data, and satellite-level multispectral data were used. Table I provides the statistical information on ground-measured vegetation parameters in the used datasets. Fig. 1 shows the locations of soybean and wheat experimental sites as well as the distribution of ground samples. The relationship between LAI and LCC ground measurements in soybean and wheat experiments is shown in Fig. 2.

A. Ground-Measured Hyperspectral Data

The soybean canopy spectra, LCC, and LAI were collected by the University of Nebraska at the US-Ne2 and US-Ne3 sites. They were collectively referred to as the Soybean-Hyper dataset. Six subsampling sites were randomly designed in each sample measurement from June to September at the US-Ne2 site in 2002 and 2004, and the US-Ne3 site in 2002, across the whole growth cycle of soybean [29]. The canopy reflectance was calculated using the radiance upwelling from the soybean canopy and the incident irradiance measured with two calibrated Ocean Optics USB2000 spectroradiometers

Authorized licensed use limited to: Aerospace Information Research Institute. Downloaded on October 19,2023 at 00:37:32 UTC from IEEE Xplore. Restrictions apply.

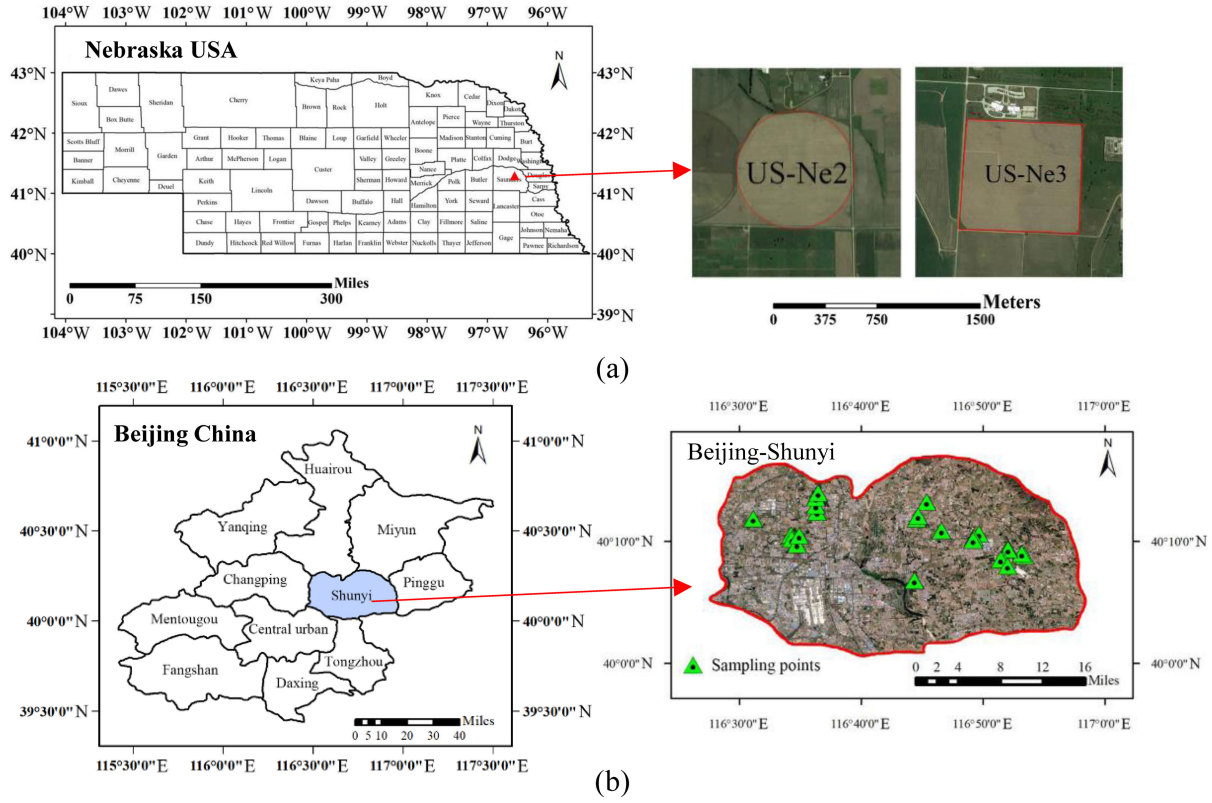


Fig. 1. Locations of (a) soybean experiment in Nebraska, USA, and (b) wheat experiment in Shunyi, Beijing, China.

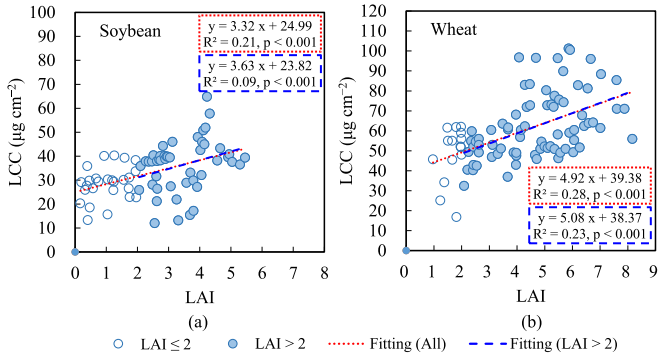


Fig. 2. Relationship between the LAI and LCC ground measurements in (a) soybean and (b) wheat experiments.

(Ocean Optics, Dunedin, FL, USA) [29], [30], [31], [32]. The wavelength range was 370–1000 nm with a resolution of 1.5 nm. Fresh leaves were collected from the soybean canopy in each subsample taken from the US-Ne2 and US-Ne3 sites. In the laboratory, the LCC was determined using acetone extraction and spectrophotometer analysis, as well as a leaf reflectance measurement with a leaf clip and an Ocean Optics USB2000 spectroradiometer [1], [29], [30], [31], [32], [33]. Subsequently, the average LCC of upper leaves in the soybean canopy was calculated. The leaf area of samples was measured using a leaf area meter (Model LI-3100 from LI Cor, Lincoln, NE, USA). Afterward, the LAI was calculated as leaf area per unit ground area [29], [34]. The soybean LCC and LAI of the matching canopy spectrum measurements in the Soybean-Hyper dataset are detailed in Table I.

B. Simulated Multispectral Data

Based on the spectral response functions of the MERIS and ETM+ sensors, the canopy hyperspectral data in the Soybean-Hyper dataset were spectrally sampled to obtain three simulated multispectral datasets (Soybean-SimMERIS, Soybean-SimMSI, and Soybean-SimETM+). Table II shows the center positions of all the simulated visible–NIR bands of MERIS, MSI, and ETM+. A total of 73 samples of the soybean multispectral dataset were simulated for each sensor.

C. Satellite Multispectral Data

1) Soybean MERIS and ETM+ Reflectance: The ESA Land Cover Climate Change Initiative project provided the MERIS full-resolution surface reflectance product, and the Landsat ETM+ surface reflectance product was available on the Google Earth Engine (GEE) cloud platform. As the soybeans at the US-Ne2 and US-Ne3 sites were uniformly growing over an area of more than 60 ha [33], [34], the average LCC and LAI obtained from ground measurements could be well matched with the MERIS and ETM+ satellite data. The reflectance of one MERIS pixel within the range of 300 × 300 m^2 and the average reflectance of the corresponding 10 × 10 ETM+ pixels at 30 m resolution were extracted using the latitude and longitude of the site as the center. In the Soybean-MERIS dataset, 21 soybean MERIS samples from the US-Ne2 site were obtained in 2004. In the Soybean-ETM+ dataset, 13 soybean ETM+ samples from the two sites were acquired in 2002 and 2004. The LAI and LCC statistics of soybean

Authorized licensed use limited to: Aerospace Information Research Institute. Downloaded on October 19,2023 at 00:37:32 UTC from IEEE Xplore. Restrictions apply.

TABLE II
VISIBLE AND NEAR-INFRARED (NIR) BAND SETTINGS OF THE MERIS, MSI, AND ETM+ SENSORS

MERIS/ENVISAT		MSI/Sentinel-2A		ETM+/Landsat	
Band	Band center (nm)	Band	Band center (nm)	Band	Band center (nm)
B1	412.5	B1	443	B1	485
B2	442.5	B2	490	B2	565
B3	490	B3	560	B3	660
B4	510	B4	665	B4	835
B5	560	B5	705		
B6	620	B6	740		
B7	665	B7	783		
B8	681.25	B8	842		
B9	708.75	B8a	865		
B10	753.75	B9	945		
B11	760.625				
B12	778.75				
B13	865				
B14	885				
B15	900				

samples at the US-Ne2 and US-Ne3 sites matching MERIS and ETM+ data are shown in Table I.

2) Wheat MSI Reflectance: MSI/Sentinel-2 reflectance data from Shunyi, Beijing, China, were matched with ground-based wheat LCC and LAI measurements. They were referred to collectively as the Wheat-MSI dataset. The Copernicus Open Access Hub portal (https://scihub.copernicus.eu/) was used to get the Sentinel-2A MSI Level-1C reflectance products. From April to May of 2016, 24 uniformly growing winter wheat fields greater than 1.0 ha were selected in the Beijing-Shunyi area, and one 10 × 10 m sample with five randomly dispersed 1 × 1 m subsamples was set up on each field [35]. More than 15 leaves were gathered from the second and third upper leaves of wheat plants in each subsample. Acetone was used to remove the chlorophyll from the leaves after measuring their area. The extracted chlorophyll was weighed and converted to LCC measures using an L6 ultraviolet–visible spectrophotometer (INESA, Shanghai, China). The LAI-2200C (Plant Canopy Analyzer, LI-COR, Lincoln, NE, USA) was used to measure LAI more than three times for each subsample. Averaging the LCC and LAI readings of five subsamples yielded the sample LCC and LAI. Four sampling measurements were taken at the jointing, booting, heading, and flowering stages of winter wheat. In the Wheat-MSI dataset, 92 valid samples with LCC and LAI values were gathered, and the details are provided in Table I.

III. METHODS

A. Definition of Hue Angle in CIE xy Chromaticity Diagram

The CIE XYZ color space is based on the CIE RGB color space and uses the three stimulus values X, Y, and Z to represent the color, with the brightness related only to the Y value. In the CIE xy chromaticity diagram (Fig. 3), color is independent of brightness, and the x and y coordinates are derived from the tristimulus values X, Y, and Z, according to the following equations [18]:

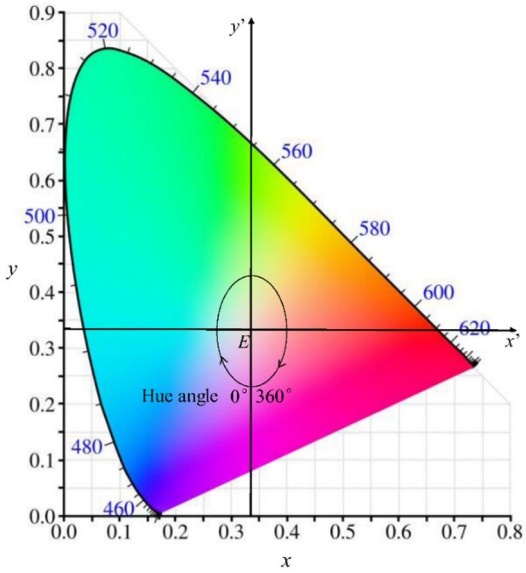


Fig. 3. Hue angle in the CIE xy chromaticity diagram. "E" is the point of equal-energy white light. The hue angle is the angle in clockwise mode between the negative y'-axis (at $x = 1/3$) and the vector from point E to a color point.

$$\mathrm{x} = \frac{\mathrm{X}}{\mathrm{X}+\mathrm{Y}+\mathrm{Z}} \tag{1}$$

$$\mathrm{y} = \frac{\mathrm{Y}}{\mathrm{X}+\mathrm{Y}+\mathrm{Z}}. \tag{2}$$

The equal-energy white light point E in the CIE xy chromaticity diagram is located at coordinates (1/3, 1/3) when X, Y, and Z are mixed in equal proportions, as shown in Fig. 3. By constructing a new coordinate system (x', y') with the origin set at the equal-energy white light point, the point (x, y) in the CIE xy chromaticity diagram corresponds to the hue angle measured clockwise in the negative direction of y'-axis. Different definitions exist for the starting position and increasing direction of the hue angle [19], [20], [21], while this definition of the hue angle helps in avoiding errors in the hue angle values of red leaves. The hue angle ranges from 0° to 360°, with positive values corresponding to the primary wavelength corresponding to the color of common leaves. Higher hue angle values indicate a color bias toward yellow and red, whereas lower values indicate a bias toward green and blue. The hue angle is calculated as

$$\text{Hue angle} = \text{ARCTAN2}\left(x - \frac{1}{3}, y - \frac{1}{3}\right) * \frac{180}{\text{pi}} + 180. \tag{3}$$

B. Calculation Algorithm of Hyperspectral Hue Angle

Given the hyperspectral reflectance of the surface object, the corresponding X, Y, and Z are calculated [18], [36], [37], [38], [39], [40]. Subsequently, the hue angle is calculated using (1)–(3). The calculation of X, Y, and Z based on surface reflectance

Authorized licensed use limited to: Aerospace Information Research Institute. Downloaded on October 19,2023 at 00:37:32 UTC from IEEE Xplore. Restrictions apply.

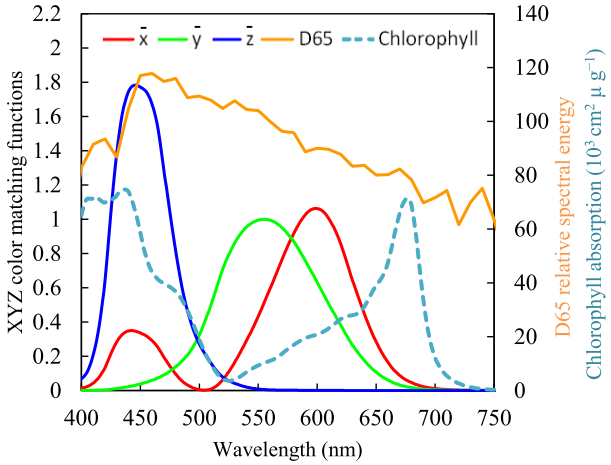


Fig. 4. CIE XYZ color matching functions, the relative spectral energy distribution of the D65 standard illuminant, and specific absorption coefficient of chlorophyll a and b.

is given by

$$\mathrm{X} = k \int S(\lambda) R(\lambda) \bar{x}(\lambda) d\lambda \tag{4}$$

$$\mathrm{Y} = k \int S(\lambda) R(\lambda) \bar{y}(\lambda) d\lambda \tag{5}$$

$$\mathrm{Z} = k \int S(\lambda) R(\lambda) \bar{z}(\lambda) d\lambda \tag{6}$$

$$k = 100 / \int S(\lambda) \bar{y}(\lambda) d\lambda \tag{7}$$

where $R(\lambda)$ denotes the surface spectral reflectance, $\bar{x}(\lambda)$, $\bar{y}(\lambda)$, and $\bar{z}(\lambda)$ are the CIE XYZ color matching functions, $S(\lambda)$ represents the relative spectral energy distribution of the illuminant and is obtained after normalizing the absolute spectral energy to a value of 1 at a wavelength of 560 nm, and k is the normalized factor, which specifies that the spectral reflectance is 100% with a maximum Y value of 100. The data of the CIE XYZ color matching functions and the relative spectral energy distribution of the D65 standard illuminant shown in Fig. 4 were downloaded from the CIE website (http://files.cie.co.at/204.xls). Fig. 4 also shows the specific absorption coefficient of chlorophyll a and b that was used in the PROSPECT leaf radiative transfer model [41] (http://teledetection.ipgp.jussieu.fr/prosail/). The effective spectral range of the CIE XYZ color matching functions covers the majority of the absorption spectrum range of chlorophyll a and b, except for the red-edge wavelength. This suggests that the hue angle extracted by visible light is able to capture the change of chlorophyll amount in plant leaves.

CIE defines the D65 illuminant as a standard illuminant for color evaluation, and it is most commonly used in industry and agriculture [36], [42]. It approximates the midday lighting environment, and its relative energy varies with wavelength (Fig. 4). The reflectance-based hue angle calculated using the D65 standard illuminant data is denoted by hue-angle$_{\mathrm{D65}}$. According to (4)–(7), the hue-angle$_{\mathrm{D65}}$ calculated based on a continuous reflectance spectrum using the D65 illuminant data is considered the true value of the hue angle. Furthermore, several water color remote sensing studies [25], [26], [27] have shown that the hue angle was calculated based on ground measurements and satellite data using wavelength-independent light source data, which was referred to as hue-angle$_{\mathrm{noD65}}$ in this study. As a result, $S(\lambda)$ in (4)–(7), which was used to calculate the hue-angle$_{\mathrm{noD65}}$, was set to 1. In the sequel, the difference between hue-angle$_{\mathrm{D65}}$ and hue-angle$_{\mathrm{noD65}}$, as well as their respective abilities for LCC estimation, was compared.

C. Calculation Method of New Multispectral Hue Angle

In [21], multispectral remote sensing data were spectrally interpolated to calculate three X, Y, and Z values and thus obtain the hue angle. For instance, in the case of calculating the multispectral X, it was the sum of all the X segments between adjacent discrete bands, and it is expressed as

$$\mathrm{X} = \sum_{i=1}^{N-1} \mathrm{X}(\lambda_i, \lambda_{i+1}) \tag{8}$$

where N is the number of effective multispectral bands between 400 and 710 nm, as referenced in [21]. In fact, the values of the CIE XYZ color matching function outside the range of 400–700 nm are negligible, as shown in Fig. 4. λ_i is the center wavelength of the ith discrete band, and $\mathrm{X}(\lambda_i, \lambda_{i+1})$ is the segment of the stimulus value X between λ_i and λ_{i+1}.

In contrast to employing the wavelength-independent illuminant in previous water remote sensing studies on existing multispectral hue angle calculation [20], [21], this study calculates the X, Y, and Z values of the discrete spectral interpolation method using the D65 standard illuminant data. Our improved calculation of $\mathrm{X}(\lambda_i, \lambda_{i+1})$ from multispectral reflectance data considering the wavelength-dependent standard illuminant factor is given by

$$\begin{aligned}\mathrm{X}(\lambda_i, \lambda_{i+1}) &= k \Bigg(R(\lambda_i) \int_{\lambda_{i-1}}^{\lambda_i} S(\lambda) \bar{x}(\lambda) \frac{(\lambda - \lambda_{i-1})}{(\lambda_i - \lambda_{i-1})} \mathrm{d}\lambda \\ &\quad + R(\lambda_{i+1}) \int_{\lambda_i}^{\lambda_{i+1}} S(\lambda) \bar{x}(\lambda) \frac{(\lambda_{i+1} - \lambda)}{(\lambda_{i+1} - \lambda_i)} \mathrm{d}\lambda \Bigg)\end{aligned} \tag{9}$$

where $R(\lambda_i)$ is the reflectivity of discrete bands with a center wavelength λ_i, $S(\lambda)$ is the relative energy distribution of the illuminant, and $\bar{x}(\lambda)$ is the color matching function for the stimulus value X. $S(\lambda)$ and $\bar{x}(\lambda)$ are continuous and do not require spectral response sampling.

By combining (8) and (9), X that was calculated using the discrete spectral interpolation method becomes an integral function of the product of the discrete band's reflectance and the corresponding weight coefficient

$$\mathrm{X} = k \sum_{i=1}^{N} w_X(i) R(\lambda_i) \tag{10}$$

where $w_{\mathrm{X}}(i)$ is the weight coefficient for the ith band and is expressed as a function of λ_i, $S(\lambda)$, and $\bar{x}(\lambda)$

$$w_{\mathrm{X}}(i = 1) = k \int_{\lambda_i}^{\lambda_{i+1}} S(\lambda) \bar{x}(\lambda) \frac{(\lambda_{i+1} - \lambda)}{(\lambda_{i+1} - \lambda_i)} \mathrm{d}\lambda \tag{11}$$

$$w_{\mathrm{X}}(1 < i < N) = k \int_{\lambda_{i-1}}^{\lambda_i} S(\lambda) \bar{x}(\lambda) \frac{(\lambda - \lambda_{i-1})}{(\lambda_i - \lambda_{i-1})} \mathrm{d}\lambda$$

Authorized licensed use limited to: Aerospace Information Research Institute. Downloaded on October 19,2023 at 00:37:32 UTC from IEEE Xplore. Restrictions apply.

TABLE III
VEGETATION INDICES (VIS) USED IN THIS STUDY

Index type	Index name	Index abbreviation	Formula[1]	Reference
Red-edge VIs	MERIS terrestrial chlorophyll index	MTCI	$(R_{\text{red-edge2}} - R_{\text{red-edge1}}) / (R_{\text{red-edge2}} + R_{\text{red-edge1}})$	[10]
	Red-edge chlorophyll index	$\text{CI}_{\text{red-edge}}$	$R_{\text{NIR}} / R_{\text{red-edge1}} - 1$	[1]
Visible–NIR VIs	Green chlorophyll index	CI_{green}	$R_{\text{NIR}} / R_{\text{green}} - 1$	[1]
	Normalized difference vegetation index	NDVI	$(R_{\text{NIR}} - R_{\text{red}}) / (R_{\text{NIR}} + R_{\text{red}})$	[43]
Visible VIs	Normalized green–red difference index	NGRDI	$(R_{\text{green}} - R_{\text{red}}) / (R_{\text{green}} + R_{\text{red}})$	[14]
	Triangular greenness index	TGI	$-0.5\,[(\lambda_{\text{red}} - \lambda_{\text{blue}})(R_{\text{red}} - R_{\text{green}}) - (\lambda_{\text{red}} - \lambda_{\text{green}})(R_{\text{red}} - R_{\text{blue}})]$	[15]

[1] Blue, green, red, red-edge1, red-edge2, and NIR respectively correspond to narrow bands at 490 nm, 560 nm, 660 nm, 710 nm, 750 nm, and 860 nm for hyperspectral data, B3, B5, B7, B9, B10, and B13 for MERIS data, and to B2, B3, B4, B5, B6, and B8a for MSI data. Blue, green, red, and NIR correspond to B1, B2, B3, and B4 for ETM+ data, respectively.

$$+\int_{\lambda_i}^{\lambda_{i+1}} S(\lambda)\bar{x}(\lambda)\frac{(\lambda_{i+1}-\lambda)}{(\lambda_{i+1}-\lambda_i)}\mathrm{d}\lambda \quad (12)$$

$$w_{\text{X}}(i=N) = k\int_{\lambda_{i-1}}^{\lambda_i} S(\lambda)\bar{x}(\lambda)\frac{(\lambda-\lambda_{i-1})}{(\lambda_i-\lambda_{i-1})}\mathrm{d}\lambda. \quad (13)$$

Similarly, the weight series w_{Y} and w_{Z} correspond to Y and Z, respectively. After X, Y, and Z are calculated based on the multispectral reflectance and band-by-band weight coefficients—w_{X}, w_{Y}, and w_{Z}, the hue angle is obtained using (1)–(3). All the $w_{\text{X}}(i)$ values for the 400- and 710-nm bands are then summed

$$\sum_{i=1}^{N} w_X(i) = k\int_{\lambda_1}^{\lambda_N} S(\lambda)\bar{x}(\lambda)\mathrm{d}\lambda = \frac{100\int_{400}^{710} S(\lambda)\bar{x}(\lambda)\mathrm{d}\lambda}{\int_{400}^{710} S(\lambda)\bar{y}(\lambda)\mathrm{d}\lambda}. \quad (14)$$

Subsequently, the sum of the w_{Y} series and that of the w_{Z} series are expressed as

$$\sum_{i=1}^{N} w_Y(i) = \frac{100\int_{400}^{710} S(\lambda)\bar{y}(\lambda)\mathrm{d}\lambda}{\int_{400}^{710} S(\lambda)\bar{y}(\lambda)\mathrm{d}\lambda} = 100 \quad (15)$$

$$\sum_{i=1}^{N} w_Z(i) = \frac{100\int_{400}^{710} S(\lambda)\bar{z}(\lambda)\mathrm{d}\lambda}{\int_{400}^{710} S(\lambda)\bar{y}(\lambda)\mathrm{d}\lambda}. \quad (16)$$

According to (14)–(16), the sums of w_X, w_Y, and w_Z should be independent of the difference of multispectral sensors, but only with the relative energy functions of the used illuminant data and the XYZ color matching functions. In the case of using the D65 standard illuminant data, the sums of w_X, w_Y, and w_Z are sets of fixed values greater than 100, equal to 100, and less than 100, respectively. When employing wavelength-independent illuminant data (i.e., $S(\lambda)$ is set to 1), the sums of w_X, w_Y, and w_Z should all be equal to 100.

The X, Y, and Z values, to calculate the multispectral hue angle, are determined by incorporating all bands within the range of 400–710 nm that are considered valid, and these used bands encompass the two boundaries of 400 and 710 nm. However, since most of the multispectral sensors do not comprise the two bands, the contributions of the 400- and 710-nm bands are lost when calculating the hue angle based on multispectral data. Fortunately, reflectance in the 400- and 710-nm bands contributes very little to the hue angle of the green or yellow colors. Therefore, the multispectral hue angle is calculated only using all the bands of the given sensor between 400 and 710 nm, excluding the 400- and 710-nm bands [21]. When $S(\lambda)$ is set as the relative energy data of D65 illuminant or fixed at 1 in (11)–(13), our proposed multispectral $\text{hue-angle}_{\text{D65}}$ and the existing multispectral $\text{hue-angle}_{\text{noD65}}$ can be obtained, respectively.

D. Chlorophyll-Related Vegetation Indices for Comparison

Six chlorophyll-related VIs were chosen for a comparative test of the LCC estimation ability using the reflectance-based hue angle. Table III shows the selected VIs, which include $\text{CI}_{\text{red-edge}}$ [1] and MTCI [10] for red-edge VIs, CI_{green} [1] and NDVI [43] for visible–NIR VIs, and NGRDI [14] and TGI [15] for visible VIs. These VIs have been previously used to estimate vegetation chlorophyll content in other studies [6], [7], [16], [44]. Red-edge bands are commonly available in hyperspectral sensors and a few multispectral sensors, while NIR and visible bands are available in most multispectral sensors. This study calculated red-edge VIs using hyperspectral and multispectral MERIS data, while visible–NIR VIs or visible VIs were calculated using multispectral ETM+ data without red-edge bands, as shown in Table III. Note that several previous studies have utilized correlation as the primary metric to demonstrate the potential of novel indices, such as $\text{CI}_{\text{red-edge}}$ [1], MTCI [10], and TGI [15], in remote sensing of vegetation parameters. The VI saturation phenomena are easily explained by its considerable nonlinear relationship with the vegetation parameter; thus, an indicator with a strong linear relationship with the vegetation parameter is preferred [10], [33], [45]. In this study, R^2 of the linear regression statistics was used to assess the potential of the tested VIs and hue angles in estimating the LCC.

IV. RESULTS

A. Test Results for Ground-Measured Hyperspectral Data

Fig. 5 shows scatter plots of the $\text{hue-angle}_{\text{D65}}$ versus $\text{hue-angle}_{\text{noD65}}$ calculated from ground-measured hyperspectral

Authorized licensed use limited to: Aerospace Information Research Institute. Downloaded on October 19,2023 at 00:37:32 UTC from IEEE Xplore. Restrictions apply.

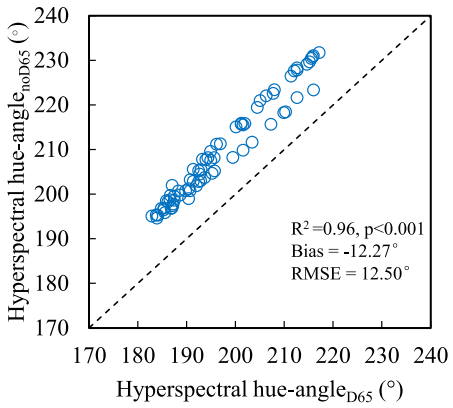


Fig. 5. Scatter plots of the hue-angle$_{D65}$ and hue-angle$_{noD65}$, calculated from ground-measured soybean canopy spectra. Hue-angle$_{D65}$ is the hue angle calculated using the D65 standard illuminant data, and hue-angle$_{noD65}$ is the hue angle calculated using wavelength-independent illuminant data.

data at canopy scales using the Soybean-Hyper datasets. The result indicates that the calculated hue-angle$_{noD65}$ tends to be yellow-red in color and is larger than the corresponding hue-angle$_{D65}$ value.

Fig. 6 shows the relationships between the LCC and the eight tested indicators using the LAI-graded soybean canopy hyperspectral data. LAI greater than 2 was used to indicate dense canopies in this study. Results show that none of the eight tested indicators calculated based on soybean canopy reflectance have strong relationships with LCC for all of the LAIs. R^2 of the MTCI-LCC regression is superior to 0.5, followed by the results of $CI_{red-edge}$ and hue-angle$_{D65}$. In dense canopies, the R^2 values of the regressions between almost all the tested indicators and LCC are improved. This demonstrates that high coverage is a critical requirement for high-quality LCC retrieval using the hue angle or VIs. For the dense canopies, the relationship between hue-angle$_{D65}$ and LCC was closer ($R^2 = 0.54$) than that of the hue-angle$_{noD65}$ and LCC ($R^2 = 0.44$) and only slightly worse than the red-edge VI—MTCI ($R^2 = 0.59$). Moreover, R^2 of the regression between the hue-angle$_{D65}$ and LCC is even slightly higher than that of the red-edge VI—$CI_{red-edge}$ ($R^2 = 0.51$) and much better than that of CI_{green} ($R^2 = 0.39$), TGI ($R^2 = 0.28$), NDVI ($R^2 = 0.24$), and NGRDI ($R^2 = 0.08$). These results suggest that the hue-angle$_{D65}$, MTCI, and $CI_{red-edge}$ are promising indicators for LCC estimation in dense soybean canopies.

B. Test Results for Simulated Multispectral Data

Table IV provides the weight coefficients used in the calculation of tristimulus values, corresponding to the center wavelength or band number of the MERIS, MSI, and ETM+ multispectral sensors using the D65 standard illuminant data and wavelength-independent illuminant data. The effect of missing the 400- and 710-nm bands on their calculation of tristimulus values for different multispectral sensors is dependent on the sensor. For the MERIS bands, the weight coefficients of the two bands at 400 and 710 nm are very low, indicating that its calculation of the tristimulus values and hue angle is reliable. For the MSI and ETM+, the w_Z value of the 400-nm band is not particularly low, potentially resulting in a greater underestimation of Z compared to X and Y. Nevertheless, given the inherent low reflectivity of most vegetation in the blue band, the absence of the 400-nm band on the ETM+ hue angle calculation might have a limited impact.

The hyperspectral hue-angle$_{D65}$ values served as the true reference values to assess the accuracy of multispectral hue angle calculations, which were determined under different illuminant data strategies using simulated multispectral datasets for Soybean-SimMERIS, Soybean-SimMSI, and Soybean-SimETM+ datasets (Fig. 7). In general, the MERIS hue-angle$_{D65}$ that was obtained was the most accurate in the simulated results of multispectral hue angles. The MSI hue angle and ETM+ hue angle calculations are generally close in accuracy, with R^2 of the ETM+ hue angle to the hyperspectral hue angle being slightly greater than that of the MSI hue angle. Moreover, the accuracy of the hue-angle$_{D65}$ calculations for simulated multispectral data of soybean canopies was found to be superior to that of hue-angle$_{noD65}$ results. Regardless of using the D65 standard illuminant data or wavelength-independent illuminant data, the calculation accuracy of the multispectral hue angle based on MERIS data was higher than that based on MSI and ETM+ data. The accuracy of multispectral hue angles for yellow or red vegetation was higher, while the overestimation of multispectral hue angles for green colors was more serious.

Fig. 8 shows R^2 of the regression relationship between the LCC and multispectral hue angle, acquired for the three multispectral sensors, as well as the two illuminant data strategies. Furthermore, the effects of canopy density on the relationship between the multispectral hue angle and LCC were compared using simulated soybean data for MERIS, MSI, and ETM+. The simulated MERIS, MSI, and ETM+ results show that, for the given sensor, the relationship between the multispectral hue-angle$_{D65}$ and the LCC was better than that between the multispectral hue-angle$_{noD65}$ and the LCC. For a given illuminant, the relationship between the MERIS hue angle and the LCC was better than that between the ETM+ hue angle and the LCC. The calculated R^2 of the MERIS hue-angle$_{D65}$ and the LCC was close to the hyperspectral hue-angle$_{D65}$ results at the canopy level (Fig. 6). R^2 of the hue-angle$_{D65}$ and LCC relationship, calculated using simulated MERIS, MSI, or ETM+ samples of the dense soybean canopies (LAI > 2), was significantly improved from 0.44 to 0.53 for the Soybean-SimMERIS dataset, from 0.4 to 0.48 for the Soybean-SimETM+ dataset, and from 0.33 to 0.42 for the Soybean-SimMSI dataset, when compared to the results of all canopy samples.

C. Test Results for Satellite Multispectral Data

Fig. 9 shows the correlation between the LCC ground measurement and the satellite-based multispectral hue angle, derived from the Soybean-MERIS, Soybean-ETM+, and Wheat-MSI datasets. The soybean results indicate a significant reduction in R^2 values of the relationship between the MERIS or ETM+ hue angle and the LCC for all soybean canopy samples, compared to the dense canopy samples (LAI > 2). Among all dense samples, the hue-angle$_{D65}$ calculated from the MERIS satellite dataset exhibited the highest correlation

Authorized licensed use limited to: Aerospace Information Research Institute. Downloaded on October 19,2023 at 00:37:32 UTC from IEEE Xplore. Restrictions apply.

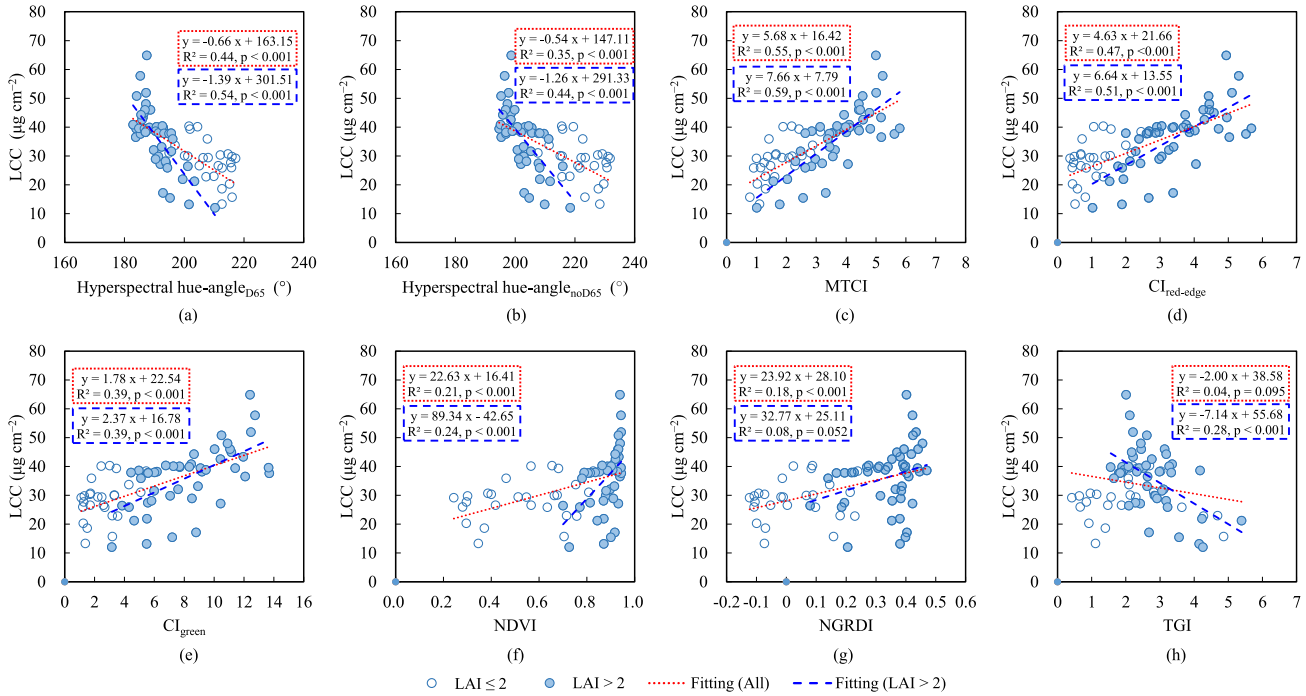


Fig. 6. Relationships between the LCC and tested remote sensing indicators, including hue angles and six vegetation indices from the soybean canopy spectral data. (a) Hyperspectral hue-angle$_{D65}$. (b) Hyperspectral hue-angle$_{noD65}$. (c) MTCI. (d) CI$_{red-edge}$. (e) CI$_{green}$. (f) NDVI. (g) NGRDI. (h) TGI.

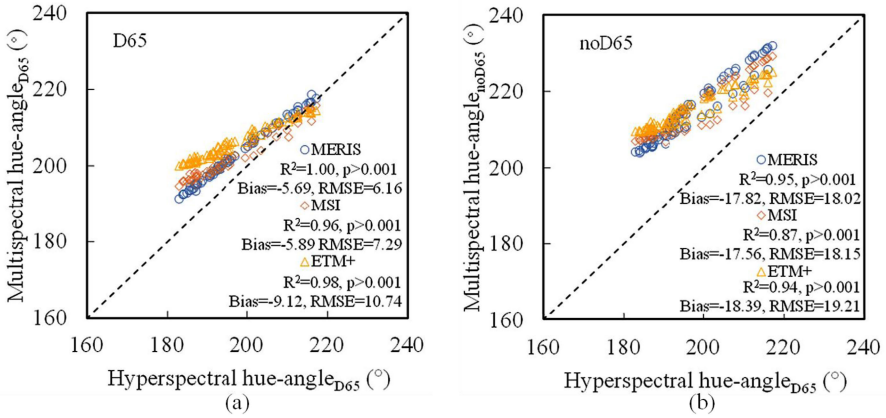


Fig. 7. Scatter plots of the hyperspectral hue-angle$_{D65}$ and multispectral hue angles calculated from simulated MERIS, MSI, and ETM+ reflectance of soybean canopies. The hyperspectral hue-angle$_{D65}$ is true hue angle to validate all calculated multispectral hue angles for three sensors (MERIS, MSI, and ETM+) and for two illuminant configurations. (a) D65 standard illuminant data and (b) wavelength-independent illuminant (noD65 illuminant) data are used in multispectral hue angle calculation.

with the LCC ($R^2 = 0.75$). Generally, for all three satellite datasets, the relationship between the hue-angle$_{D65}$ and the LCC was better (or not worse) than the results of the hue-angle$_{noD65}$.

Table V shows R^2 of the regression between the LCC and all tested indicators, including the two hue angles and the six VIs. In the Soybean-MERIS and Soybean-ETM+ datasets, the relationship between hue angle or VI and soybean LCC was stronger in dense canopies (LAI > 2) than in all canopies (LAI > 0). The Wheat-MSI dataset also showed a substantial correlation between the multispectral hue angle and LCC. Because the proportion of sparse samples is small and the low LCC values in sparse samples are lacking in dense samples (Fig. 2), R^2 of the hue angle-1 of dense samples or even slightly improved. In general, the results of the MERIS, ETM+, and MSI data show that the satellite-based hue angle also had a higher and more stable LCC correlation compared with the tested visible–NIR VIs—CI$_{green}$ and NDVI—and visible VIs—NGRDI and TGI. The MERIS and MSI hue angles, especially hue-angle$_{D65}$, demonstrate the ability to estimate the LCC close to the red-edge VIs—MTCI and CI$_{red-edge}$.

V. Discussion

This study seeks to introduce hue angle into multispectral remote sensing of vegetation because its potential chlorophyll recognition capacity is supported by a knowledge of the evolution of the human eye's recognition of green vegetation and the design of the CIE XYZ color space. Compared to multidimensional color indicators, such as X, Y, and Z in the CIE XYZ color space and x and y in the CIE xy chromaticity diagram [24], [46], the hue angle defined in the CIE xy chromaticity diagram is a single-dimensional indicator that

Authorized licensed use limited to: Aerospace Information Research Institute. Downloaded on October 19,2023 at 00:37:32 UTC from IEEE Xplore. Restrictions apply.

TABLE IV

WEIGHT COEFFICIENTS FOR THE CALCULATION OF X, Y, AND Z FOR THE MERIS, MSI, AND ETM+ SENSORS USING THE D65 ILLUMINANT DATA AND THE WAVELENGTH-INDEPENDENT ILLUMINANT DATA

Sensor	Illuminant	Weights for the calculation of the tristimulus values											
MERIS		R_λ	R_{400}	$R_{412.5}$	$R_{442.5}$	R_{490}	R_{510}	R_{560}	R_{620}	R_{665}	$R_{681.25}$	$R_{708.75}$	R_{710}	Total
		Band		B1	B2	B3	B4	B5	B6	B7	B8	B9		
	D65	w_X	0.123	2.492	11.116	4.180	3.762	31.563	35.027	5.941	0.624	0.126	0.003	95.0
		w_Y	0.003	0.095	1.830	6.022	23.380	45.811	20.307	2.299	0.227	0.046	0.001	100.0
		w_Z	0.586	12.096	60.034	31.073	4.132	0.619	0.022	0.000	0.000	0.000	0.000	108.6
	noD65	w_X	0.140	2.681	10.182	3.582	3.537	32.462	39.146	7.164	0.798	0.174	0.004	99.9
		w_Y	0.004	0.101	1.598	5.349	21.772	45.644	22.429	2.770	0.290	0.063	0.001	100.0
		w_Z	0.664	13.011	54.660	26.819	3.792	0.585	0.024	0.000	0.000	0.000	0.000	99.6
MSI		R_λ	R_{400}	R_{443}	R_{490}	R_{560}	R_{665}	R_{705}	R_{710}					
		Band		B1	B2	B3	B4	B5						
	D65	w_X	1.937	11.869	6.792	47.646	26.312	0.381	0.011					94.9
		w_Y	0.073	1.872	22.701	61.191	14.033	0.138	0.004					100.0
		w_Z	9.396	63.744	33.597	1.808	0.013	0.000	0.000					108.6
	noD65	w_X	2.089	10.978	6.043	50.246	29.987	0.500	0.015					99.9
		w_Y	0.078	1.640	20.882	61.474	15.751	0.182	0.006					100.0
		w_Z	10.127	58.571	29.161	1.678	0.014	0.000	0.000					99.6
ETM+		R_λ	R_{400}	R_{485}	R_{565}	R_{660}	R_{710}							
		Band		B1	B2	B3								
	D65	w_X	7.574	13.530	47.739	25.632	0.472							94.9
		w_Y	0.849	24.541	61.263	13.187	0.172							100.0
		w_Z	39.365	66.979	2.186	0.011	0.000							108.5
	noD65	w_X	7.318	12.282	50.335	29.310	0.611							99.9
		w_Y	0.759	22.576	61.567	14.887	0.222							100.0
		w_Z	37.760	59.743	2.020	0.012	0.000							99.5

D65 indicates using the D65 standard illuminant data and noD65 indicates using wavelength-independent illuminant data.

is easier to use in representing the color of plant leaves. Previous studies on the estimation of the plant chlorophyll status using color characteristics relied primarily on visible cameras or color meters in the laboratory and in the field [47], [48], [49]. Reflectance-based hue angle has been used in water color remote sensing [25], [26], [27]. However, the usage of standard illuminant data is not taken into consideration in this reflectance-based hue angle calculation, which contradicts the original design of the CIE XYZ color space. Furthermore, it has not been applied in vegetation remote sensing, particularly when an effective indicator for estimating LCC based on multispectral data without red-edge bands is required. This study focuses on developing the new multispectral hue angle calculation method employing D65 standard illuminant data (multispectral hue-angle$_{D65}$) and evaluating its LCC estimation potential based on the commonly used nonred-edge sensors, especially at canopy and satellite scales. Our results demonstrate that the CIE XYZ hue angle calculated by using standard illuminant data can be employed as a novel visible indicator for multispectral remote sensing of leaf chlorophyll status. Furthermore, when compared to hue angle results from another widely used color space—the CIELAB (Fig. 10), the hue angle derived from the CIE XYZ color space (Fig. 6) appears to be more competitive in estimating plant chlorophyll. It is worth noting that to own a perceptually uniform color difference, the CIE XYZ color space, as a linear color space, is nonlinearly transformed into the CIELAB color space [50], [51]. This transformation may produce a poorer correlation between the

Authorized licensed use limited to: Aerospace Information Research Institute. Downloaded on October 19,2023 at 00:37:32 UTC from IEEE Xplore. Restrictions apply.

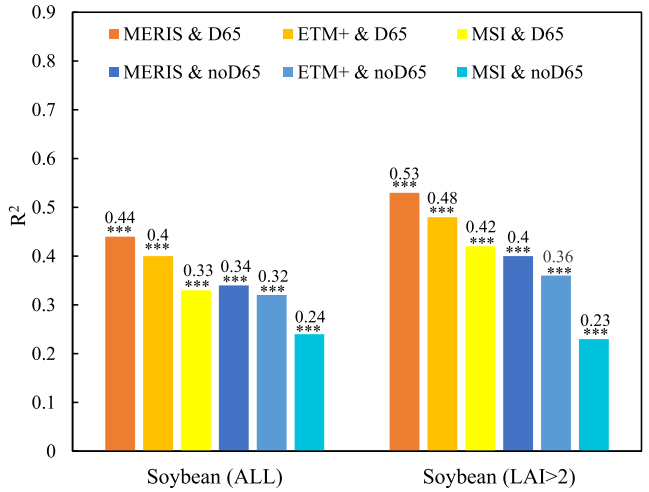


Fig. 8. R^2 values of the regression between the LCC and multispectral hue angles, calculated from simulated MERIS, ETM+, and MSI reflectance of soybean canopies. D65 indicates using the D65 standard illuminant data and noD65 indicates using wavelength-independent illuminant data. *** indicates significance at the 0.001 level.

TABLE V

R^2 OF THE REGRESSION RELATIONSHIP BETWEEN LCC AND SATELLITE-BASED VEGETATION INDICES

Index	Soybean-MERIS		Soybean-ETM+		Wheat-MSI	
	All	LAI>2	All	LAI>2	All	LAI>2
Hue-angle$_{D65}$	0.69***	0.75***	0.24	0.53*	0.55***	0.53***
Hue-angle$_{noD65}$	0.52***	0.75***	0.23	0.45	0.41***	0.37***
MTCI	0.79***	0.86***	-	-	0.32***	0.23***
$CI_{red-edge}$	0.59***	0.77***	-	-	0.15***	0.07*
CI_{green}	0.61***	0.71***	0.24	0.27	0.05*	0.00
NDVI	0.11	0.39*	0.17	0.36	0.16***	0.04
NGRDI	0.11	0.29*	0.19	0.22	0.09**	0.01
TGI	0.22*	0.69***	0.1	0.03	0.07**	0.21***

***, **, and * indicate significance at the 0.001, 0.01, and 0.05 levels, respectively.

CIELAB hue angle and the LCC than the CIE XYZ hue angle and the LCC. The findings are helpful in promoting the practicability of this new approach in vegetation multispectral remote sensing.

As described in (11)–(13), this study developed the algorithm for calculating tristimulus weight coefficient for a given multispectral sensor using standard illuminant data and provided the coefficients for MERIS, MSI, and ETM+ sensors so that their multispectral hue angle can be easily computed from the visible bands. When calculating the reflectance-based hue angle, it is important to consider whether standard illuminant data are used. This study highlights that the hue-angle$_{noD65}$ is higher than the true hue-angle$_{D65}$, which is not observed by previous reflectance-based hue angle studies [19], [20], [21]. The relative energy of the standard illuminant changes with the wavelength and is used as the weight of each band in the calculation of X, Y, and Z. When using D65 standard illuminant data, the illuminant weights corresponding to the vegetation reflectance of blue or green wavelengths (especially blue) are greater than those corresponding to the red reflectance. Therefore, the calculated hue-angle$_{noD65}$ appears more yellow-red than the corresponding hue-angle$_{D65}$. For green vegetation, the values of the hyperspectral hue-angle$_{noD65}$ are nearly 10° higher than those of the hyperspectral hue-angle$_{D65}$, as shown in Fig. 5. Moreover, the variations of the band weights of X, Y, and Z calculations under different illuminant data strategies explain why the hue-angle$_{noD65}$ has a higher calculation than the hue-angle$_{D65}$. However, there is a scaling issue in the weight coefficients obtained by different methods. As shown in Table IV, the band weight sum values of approximately 95, 100, and 108.5 for X, Y, and Z calculation, respectively, using D65 standard illuminant data are inconsistent with the fixed sum value of 100 under the wavelength-independent illuminant data strategy. Furthermore, in the results obtained in [21], the fixed weight sum for X, Y, or Z is 106 under the wavelength-independent illumination data strategy. The weights were normalized to account for the scaling differences in band weight coefficients. Using the MERIS sensor as an example in Fig. 11, the normalized weights for calculating the hue-angle$_{noD65}$ are in line with those normalized values based on the results in [21]. Notably, the normalized weight of the blue-band reflectance using the D65 standard illuminant data is larger than that using the wavelength-independent illuminant data, which results in a higher value of the hue-angle$_{noD65}$ than that of hue-angle$_{D65}$.

This study reveals that the ability of the reflectance-based hue angle to reflect the chlorophyll status of plants differs depending on whether standard illuminant data is used or not. As shown in the above results, the relationship between the LCC and the hue angle calculated using D65 standard illuminant data is more sensitive than the hue-angle$_{noD65}$. The CIE xy chromaticity diagram is designed based on an illuminant similar to the D65 standard illuminant, and the green part of the chromaticity diagram has a broader hue angle range than the yellow part [38], [42]. However, the calculated hue-angle$_{noD65}$ for green leaves tends to become yellow, causing saturation at medium and high LCC. This saturation issue can limit the ability of hue-angle$_{noD65}$ to estimate the LCC accurately. Human eyes generally recognize colors in the sunlight, and hue-angle$_{D65}$ is better than hue-angle$_{noD65}$ at representing the vegetation colors recognized by human eyes. This finding suggests that the human eye recognizes the chlorophyll status of plants under light circumstances similar to sunlight. The comparison results of vegetation hue angles based on different illuminant data strategies presented in this study also serve as a useful reference for applying hue angles of other objects, such as water, soil, and fruits.

Our proposed multispectral hue angle, such as the VIs, is viewed as a transformed form of the vegetation visible reflectance spectrum, and this transformation is established using current color space knowledge. Red-edge VIs have been considered to have high accuracy in vegetation chlorophyll retrieval [6], [10], [12], which is consistent with the findings of this study. The obtained comparison results from the canopy and satellite datasets show that the sensitivity of hue angle to the LCC appears weaker or close to the two tested red-edge VIs, but higher than the four tested visible–NIR and visible VIs. Furthermore, the soybean LCC estimation model

Authorized licensed use limited to: Aerospace Information Research Institute. Downloaded on October 19,2023 at 00:37:32 UTC from IEEE Xplore. Restrictions apply.

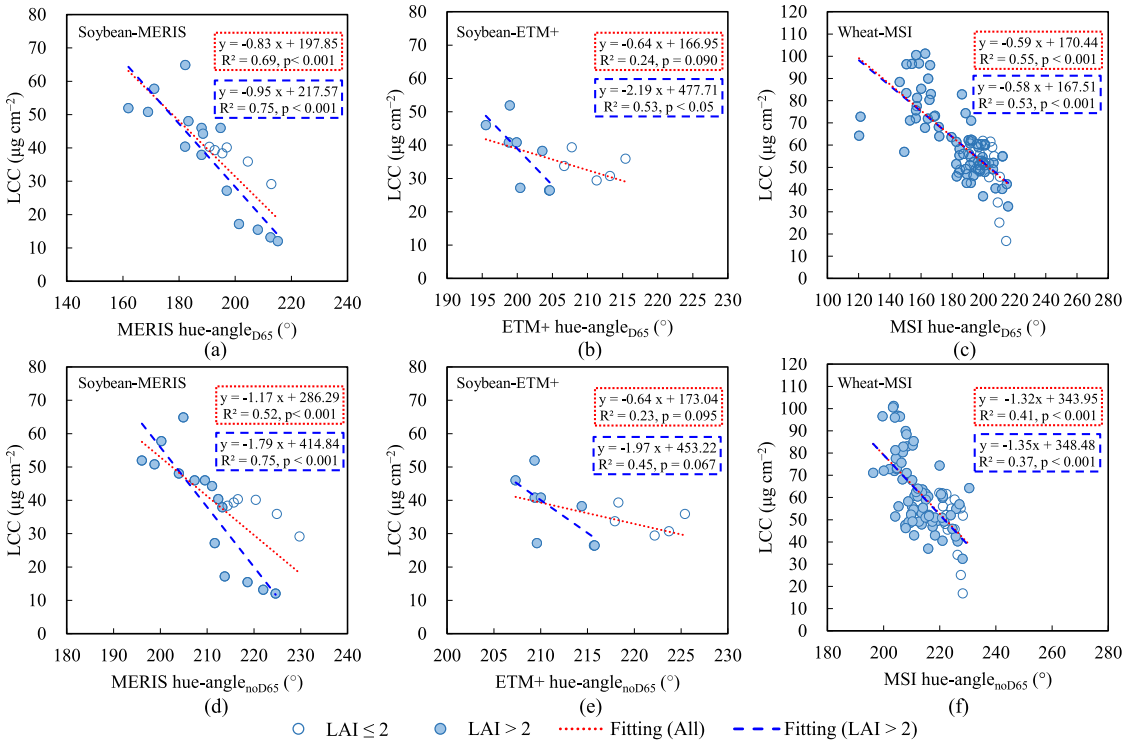


Fig. 9. Relationships between the LCC and multispectral hue angles, calculated from MERIS, ETM+, and MSI satellite data. (a) Soybean hue-angle$_{D65}$ based on MERIS data. (b) Soybean hue-angle$_{D65}$ based on ETM+ data. (c) Wheat hue-angle$_{D65}$ based on MSI data. (d) Soybean hue-angle$_{noD65}$ based on MERIS data. (e) Soybean hue-angle$_{noD65}$ based on ETM+ data. (f) Wheat hue-angle$_{noD65}$ based on MSI data.

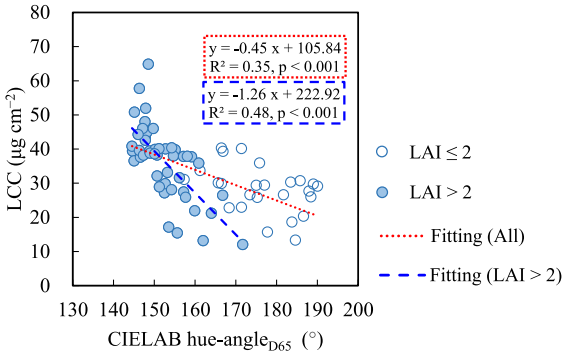


Fig. 10. Relationships between the LCC and CIELAB hue angles calculated from the soybean canopy spectral data.

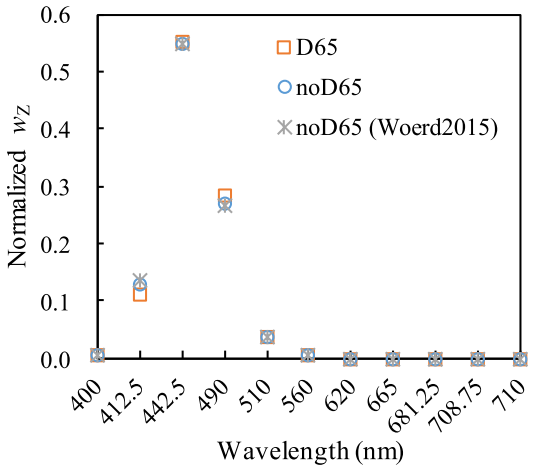


Fig. 11. Normalized weight coefficients for the calculation of the stimulus value Z (normalized w_Z), corresponding to the central wavelengths of the MERIS bands. The Woerd2015 represents the result obtained in [21].

trained on ground spectrally resampled reflectance was applied to satellite data using the MERIS sensor as an example (Fig. 12), and it is discovered that the LCC estimation accuracy using the red-edge VI—MTCI is still slightly better than our proposed hue-angle$_{D65}$, which is better than the existing hue-angle$_{noD65}$ and the popular nonred-edge VI—NDVI. Satellite- or UAV-based multispectral remote sensing has been a common solution for large-scale plant chlorophyll monitoring [52], [53]. However, the red-edge VIs are inapplicable to the multispectral sensors having no red-edge bands. The hue angle, which is mainly calculated based on the visible bands, serves as a feasible chlorophyll indicator for such sensors. In fact, the empirical regression relationship between VIs and LCC in a given area is typically dependent on the unique vegetation type or soil type [6], [45], which could result in large R^2, as we found in the soybean or wheat samples. Advanced machine learning methods, such as neural network, that are based on vegetation radiative transfer models or huge training datasets have been regarded as suitable or estimating vegetation parameters across areas and vegetation types [54], [55]. Integrating VIs into the training of machine learning algorithms for vegetation parameter retrieval has also been demonstrated to be advantageous [56], [57]. Reflectance-based hue angles determined from visible bands can be useful in monitoring regional or perhaps global LCC using empirical or more complicated machine learning techniques.

It should be noted that vegetation sparseness affects the canopy reflectance [9], [60], severely reducing the accuracy of LCC estimation using VIs at the canopy

Authorized licensed use limited to: Aerospace Information Research Institute. Downloaded on October 19,2023 at 00:37:32 UTC from IEEE Xplore. Restrictions apply.

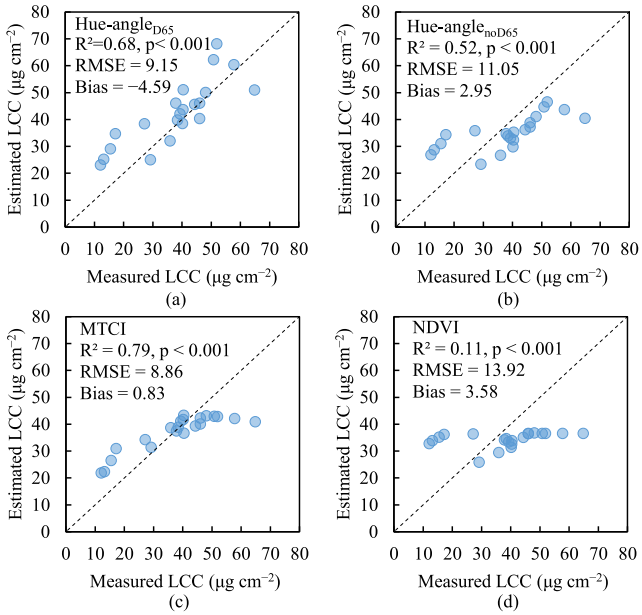


Fig. 12. Comparison between the measured LCC and that estimated from the Soybean-MERIS dataset using the remote sensing indicator-LCC models trained on the Soybean-SimMERIS dataset. (a) Hue-angle$_{D65}$. (b) Hue-angle$_{noD65}$. (c) MTCI. (d) NDVI.

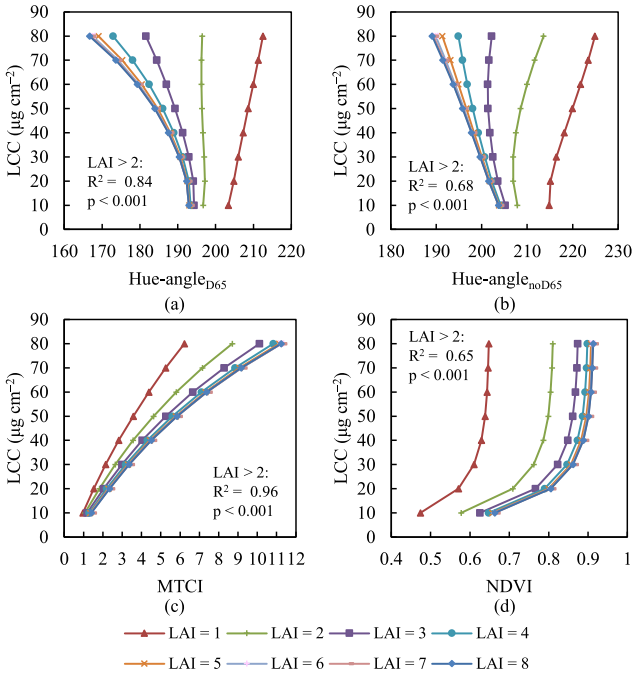


Fig. 13. Relationship of the LCC with (a) hue-angle$_{D65}$, (b) hue-angle$_{noD65}$, (c) MTCI, and (d) NDVI at various LAIs based on simulated MERIS data from the PROSAIL simulations from a nadir view. Except for LAI and LCC, other parameters of the PROSAIL model were set to fixed values (leaf water content = 0.01 g cm^{-2}, leaf dry matter content = 0.003 g cm^{-2}, N = 1.55, average leaf inclination angle = 57°, and sun zenith angle = 30°).

scale [7], [15], [56], [59], [60]. The lower the spatial resolution of remote sensing data, the more mixed pixels of vegetation and nonvegetation landscape [9], [16], [33], which brings greater uncertainty to the large-scale LCC estimation using the VIs. This is also confirmed in this study. Furthermore, it is deduced that the correlation between our proposed hue angle and the LCC is more significant in a dense canopy than in a spare canopy. As shown in Fig. 2, the correlation between ground-measured LAI and LCC in the soybean and wheat experiments is poor, especially in the case of high LAI, R^2 between LAI and LCC in the soybean dataset is near to 0, indicating that our above findings based on the tested data are rather reliable. With the better decoupling of LCC and LAI of samples, this may be well illustrated by simulating the relationship between LCC and VIs at various LAIs using a plant radiative transfer model—PROSAIL model [11], [35], [45], [59], and Fig. 13 provides a simulation example of the two hue angles, MTCI, and NDVI. Although both the hue angles and the two VIs in a fixed LAI case exhibit a clear association with LCC, these correlations are influenced by changes in LAI, especially when LAI is low. Furthermore, as shown in Fig. 13(d), changes in LAI have a greater impact on the nonlinear relationship between the NDVI and LCC, which may cause the more erroneous LCC estimation based on canopy- and satellite-level data. Fig. 13 shows that the VIs and the hue angles have a more reliable connection with LCC in a dense canopy than in a sparse canopy. This is because, as the LAI increases, the contribution of the soil background to canopy reflectance decreases greatly [5], [60]. Even with a high LAI, the sensitivity of these indicators to LCC varies. The existing hue angle becomes saturated quickly at middle LCC when LAI is 3, and the NDVI has the saturate for all LAIs. In dense canopies (LAI > 2), the MTCI and our suggested multispectral hue angle (hue-angle$_{D65}$) are more sensitive to LCC than the existing hue angle (hue-angle$_{noD65}$) and NDVI. The vegetation spectrum simulations with ideal LCC and LAI decoupling support our test results (Figs. 6, 8, and 9, and Table V). Of course, the decoupling of LCC and canopy parameters, including not only LAI in real canopies, based on nondense canopy reflectance or derived indicators like our proposed hue angle, has remained a very challenging area of research [44].

Our finding suggests that high-density canopy pixels must be identified first in order to generate quality labels for high-accuracy LCC estimation based on a reflectance-based hue angle, as these high-quality labels are critical for LCC-based vegetation applications. Fortunately, identifying pixels primarily composed of dense canopies can be easily performed using NDVI, high-resolution images, or other land cover prior knowledge [61]. Despite the fact that this study did not look into how to improve LCC estimation of sparse vegetation, several studies have investigated various strategies to reduce the impact of soil on LCC estimation models based on reflectance or chlorophyll-related VIs for sparse canopies, such as using selecting nonnoon observations [45], multiangle observations [62], advanced vegetation-soil spectral separation (3SV) method for hyperspectral data [63], or building VIs based on canopy scattering coefficients from spectral invariants theory [60]. The use of our proposed reflectance-based hue angle into these strategies could potentially help to improve the LCC estimation based on multispectral data without red-edge bands in all canopies or over the whole vegetation stages.

Uncertainty in atmospheric correction, particularly due to inaccurate aerosol correction, is another significant concern in satellite-level remote sensing of vegetation [64], [65], [66]. To demonstrate the effect of atmospheric correction errors

Authorized licensed use limited to: Aerospace Information Research Institute. Downloaded on October 19,2023 at 00:37:32 UTC from IEEE Xplore. Restrictions apply.

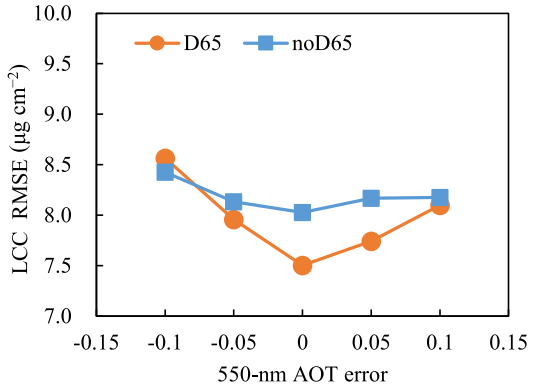


Fig. 14. Cross-validated RMSE of soybean LCC estimation based on hue angles against the 550-nm AOT errors in atmospheric correction. The truth value of 550-nm AOT is 0.2. The AOT errors of −0.1, −0.05, 0, 0.05, and 0.1 correspond to the AOT inputs of 0.1, 0.15, 0.2, 0.25, and 0.3, respectively. A tenfold cross validation is done using MATLAB's crossvalind function at the 0.001 significance level.

on LCC estimation using different hue angles, atmospheric correction simulations were conducted using ground-measured soybean reflectance data, and the LCC estimation using the two different hue angles was cross-validated (Fig. 14). Satellite-measured canopy reflectance with aerosol correction errors, simulated by the Second Simulation of the Satellite Signal in the Solar Spectrum (6S) model [67], was applied to the hue angle-LCC model without atmospheric correction errors. It is important to mention that the inaccuracy of the atmospheric correction has a higher impact on the LCC estimation performance of the hue-angle$_{D65}$ than that of hue-angle$_{noD65}$ (Fig. 14). This is because AOT errors significantly affect the correction of atmospheric effects in the blue region [68], [69], which is also shown in Fig. 15, and the blue reflectance has a greater weight for calculating the hue-angle$_{D65}$ compared with hue-angle$_{noD65}$. Furthermore, the overestimation of the AOT has less influence on the LCC estimation using the reflectance-based hue angle than the underestimation of AOT in atmospheric correction. Naturally, robust atmospheric correction algorithms, clear air conditions, and low-altitude UAV flights are conducive to an accurate atmospheric correction of multispectral images [70], [71], which ensures the effectiveness of LCC estimation by the multispectral hue angle.

The difference in the band setting of satellite- or UAV-based multispectral sensors should be considered in the calculation of the hue angle and its application. The obtained results show that there is a systematic deviation of the multispectral vegetation hue angle from the true value of the hyperspectral calculated hue angle. The multispectral sensors generally lack a band at 400 nm, causing the multispectral hue angle to be systematically high. Bands with a wavelength slightly greater than 710 nm or less than 400 nm can also be used as effective bands for (4)–(13) to calculate the multispectral hue angle, except that the weighting factors corresponding to these bands will be very small. In this study, visible spectra were obtained only using a simple linear interpolation of multispectral data between 400 and 710 nm as the basis for multispectral hue angle calculation. Moreover, it is necessary to assess whether these bands at wavelengths higher than

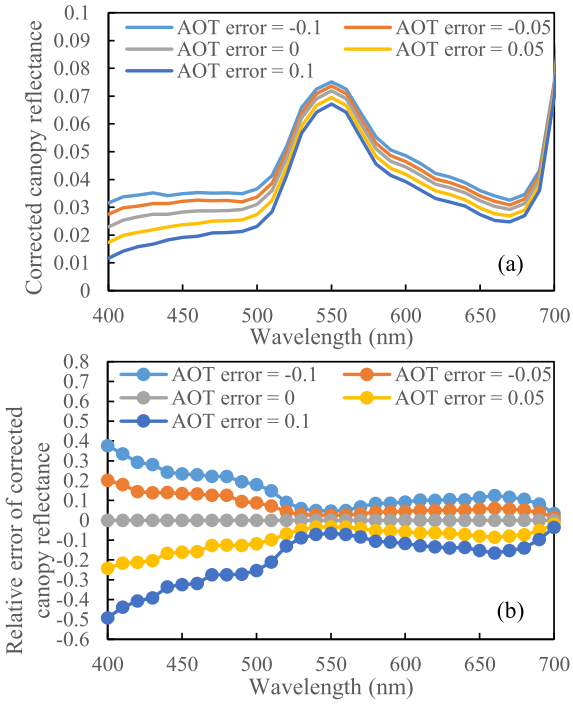


Fig. 15. (a) Atmospherically corrected reflectance of a soybean canopy and (b) its relative errors due to aerosol input errors.

710 nm or lower than 400 nm contribute to the accurate reconstruction of vegetation visible spectra, particularly when using more sophisticated spectral reconstruction methods. The development of advanced spectral reconstruction methods, such as the fusion of multispectral and hyperspectral images [72], presents an opportunity to enhance the utility of the multispectral hue angle. Furthermore, inconsistencies exist in the hue angles calculated from different multispectral sensors, such as the MERIS, MSI, and ETM+ sensors. Normalization of multisensor hue angle products is required when carrying out vegetation monitoring applications based on hue angle products from different multispectral sensors. This concept is similar to the NDVI normalization for different sensors [73], [74]. Currently, the correction method of the multisensor hue angles based on a water spectral simulation dataset in water color application studies [21], [25] can be used as a reference. New normalization schemes, such as the selection of vegetation spectral benchmark datasets to establish the relationship between multispectral hue angle and hyperspectral hue angle or between hue angle products from different multispectral sensors, should be considered for monitoring vegetation LCC dynamics with higher temporal resolution.

VI. Conclusion

To design an effective chlorophyll-related indicator from multispectral data without nonred-edge bands, this study developed a new multispectral clockwise-defined hue angle calculation method employing standard illuminant data, which is line with the CIE XYZ color space, as well as the sensitivity of LCC to our proposed hue angles at canopy and satellite scales was investigated. For the first time, the tristimulus weight coefficients for MERIS, MSI, and ETM+ sensors were provided using the newly developed algorithm, making it easy

Authorized licensed use limited to: Aerospace Information Research Institute. Downloaded on October 19,2023 at 00:37:32 UTC from IEEE Xplore. Restrictions apply.

to calculate their multispectral hue angles from the visible bands using D65 standard illuminant data. The results revealed that using wavelength-independent illuminant data or discrete bands overcalculated the hue angle. Our proposed multispectral hue angle showed better sensitivity to the LCC than the existing hue angle calculated using wavelength-independent illuminant data and the tested visible–NIR and visible VIs and performed slightly worse or close to the red-edge MTCI. The presented evaluation on the potential of our proposed multispectral hue angle for LCC estimation provides a critical foundation for monitoring leaf chlorophyll status using satellite- and UAV-based nonred-edge sensors. Future research should include studies on hue angle testing in various canopies (both crops and forests), using real data from more sensors with various atmospheric effects, the normalization of multisensor hue angles, and novel vegetation monitoring applications, such as detecting the canopy chlorophyll vertical distribution by using multispectral hue angles.

ACKNOWLEDGMENT

The authors appreciate the nonpublicly shared soybean data provided by the Center for Advanced Land Management Information Technologies (CALMIT), University of Nebraska-Lincoln, Lincoln, NE, USA. They would like to thank Dr. Xianfeng Zhou of Hangzhou Dianzi University for providing the measured data of wheat LCC and LAI in Shunyi, Beijing, China. They also thank E. F. Vermote, D. Tanre, J. L. Deuzé, M. Herman, and J.-J. Morcrette for the 6S model code, and F. Baret, J.-B. Féret, and W. Verhoef for the PROSPECT and PROSAIL model code.

REFERENCES

[1] A. A. Gitelson, Y. Gritz, and M. N. Merzlyak, "Relationships between leaf chlorophyll content and spectral reflectance and algorithms for non-destructive chlorophyll assessment in higher plant leaves," *J. Plant Physiol.*, vol. 160, no. 3, pp. 271–282, Jan. 2003.

[2] H. Croft, J. M. Chen, X. Luo, P. Bartlett, B. Chen, and R. M. Staebler, "Leaf chlorophyll content as a proxy for leaf photosynthetic capacity," *Global Change Biol.*, vol. 23, no. 9, pp. 3513–3524, Sep. 2017.

[3] D. E. Pabon-Moreno, M. Migliavacca, M. Reichstein, and M. D. Mahecha, "On the potential of Sentinel-2 for estimating gross primary production," *IEEE Trans. Geosci. Remote Sens.*, vol. 60, 2022, Art. no. 4409412.

[4] A. Pinar and P. J. Curran, "Technical note grass chlorophyll and the reflectance red edge," *Int. J. Remote Sens.*, vol. 17, no. 2, pp. 351–357, Jan. 1996.

[5] G. A. Blackburn, "Hyperspectral remote sensing of plant pigments," *J. Experim. Botany*, vol. 58, no. 4, pp. 855–867, Nov. 2006.

[6] J. G. P. W. Clevers and A. Gitelson, "Remote estimation of crop and grass chlorophyll and nitrogen content using red-edge bands on Sentinel-2 and -3," *Int. J. Appl. Earth Observ. Geoinf.*, vol. 23, no. 1, pp. 344–351, 2013.

[7] P. J. Zarco-Tejada, A. Hornero, P. S. A. Beck, T. Kattenborn, P. Kempeneers, and R. Hernández-Clemente, "Chlorophyll content estimation in an open-canopy conifer forest with sentinel-2A and hyperspectral imagery in the context of forest decline," *Remote Sens. Environ.*, vol. 223, pp. 320–335, Mar. 2019.

[8] G. le Maire, C. François, and E. Dufrêne, "Towards universal broad leaf chlorophyll indices using PROSPECT simulated database and hyperspectral reflectance measurements," *Remote Sens. Environ.*, vol. 89, no. 1, pp. 1–28, Jan. 2004.

[9] Y. Xiao, W. Zhao, D. Zhou, and H. Gong, "Sensitivity analysis of vegetation reflectance to biochemical and biophysical variables at leaf, canopy, and regional scales," *IEEE Trans. Geosci. Remote Sens.*, vol. 52, no. 7, pp. 4014–4024, Jul. 2014.

[10] J. Dash and P. J. Curran, "The MERIS terrestrial chlorophyll index," *Int. J. Remote Sens.*, vol. 25, no. 23, pp. 5403–5413, Dec. 2004.

[11] D. Haboudane, J. R. Miller, N. Tremblay, P. J. Zarco-Tejada, and L. Dextraze, "Integrated narrow-band vegetation indices for prediction of crop chlorophyll content for application to precision agriculture," *Remote Sens. Environ.*, vol. 81, nos. 2–3, pp. 416–426, Aug. 2002.

[12] Z. Malenovský et al., "Retrieval of spruce leaf chlorophyll content from airborne image data using continuum removal and radiative transfer," *Remote Sens. Environ.*, vol. 131, pp. 85–102, Apr. 2013.

[13] K. Bi, S. Xiao, S. Gao, C. Zhang, N. Huang, and Z. Niu, "Estimating vertical chlorophyll concentrations in maize in different health states using hyperspectral LiDAR," *IEEE Trans. Geosci. Remote Sens.*, vol. 58, no. 11, pp. 8125–8133, Nov. 2020.

[14] R. L. Pearson and L. D. Miller, "Remote mapping of standing crop biomass for estimation of the productivity of the short grass Prairie," in *Proc. 8th Int. Symp. Remote Sens. Environ.* Ann Arbor, MI, USA: Univ. Michigan, 1972, pp. 1357–1381.

[15] E. R. Hunt, P. C. Doraiswamy, J. E. Mcmurtrey, C. S. T. Daughtry, E. M. Perry, and B. Akhmedov, "A visible band index for remote sensing leaf chlorophyll content at the canopy scale," *Int. J. Appl. Earth Observ. Geoinf.*, vol. 21, pp. 103–112, Apr. 2013.

[16] P. J. Zarco-Tejada, J. R. Miller, T. L. Noland, G. H. Mohammed, and P. H. Sampson, "Scaling-up and model inversion methods with narrowband optical indices for chlorophyll content estimation in closed forest canopies with hyperspectral data," *IEEE Trans. Geosci. Remote Sens.*, vol. 39, no. 7, pp. 1491–1507, Jul. 2001.

[17] X. Zhou et al., "Assessment of leaf chlorophyll content models for winter wheat using Landsat-8 multispectral remote sensing data," *Remote Sens.*, vol. 12, no. 16, p. 2574, Aug. 2020.

[18] *CIE, Commission Internationale de l'Eclairage Proceedings, 1931*, Cambridge Univ. Press, Cambridge, U.K, 1932.

[19] M. R. Wernand, A. Hommersom, and H. J. van der Woerd, "MERIS-based ocean colour classification with the discrete Forel–Ule scale," *Ocean Sci.*, vol. 9, no. 3, pp. 477–487, May 2013.

[20] S. Wang, J. Li, Q. Shen, B. Zhang, F. Zhang, and Z. Lu, "MODIS-based radiometric color extraction and classification of inland water with the Forel–Ule scale: A case study of Lake Taihu," *IEEE J. Sel. Topics Appl. Earth Observ. Remote Sens.*, vol. 8, no. 2, pp. 907–918, Feb. 2015.

[21] H. Woerd and M. Wernand, "True colour classification of natural waters with medium-spectral resolution satellites: SeaWiFS, MODIS, MERIS and OLCI," *Sensors*, vol. 15, no. 10, pp. 25663–25680, Oct. 2015.

[22] T. T. Alföldi and J. C. Munday, "Water quality analysis by digital chromaticity mapping of Landsat data," *Can. J. Remote Sens.*, vol. 4, no. 2, pp. 108–126, Aug. 1978.

[23] A. C. Madeira, A. Ferreira, A. de Varennes, and M. I. Vieira, "SPAD meter versus tristimulus colorimeter to estimate chlorophyll content and leaf color in sweet pepper," *Commun. Soil Sci. Plant Anal.*, vol. 34, nos. 17–18, pp. 2461–2470, Nov. 2003.

[24] A. Agarwal and S. D. Gupta, "Assessment of spinach seedling health status and chlorophyll content by multivariate data analysis and multiple linear regression of leaf image features," *Comput. Electron. Agricult.*, vol. 152, pp. 281–289, Sep. 2018.

[25] H. van der Woerd and M. Wernand, "Hue-angle product for low to medium spatial resolution optical satellite sensors," *Remote Sens.*, vol. 10, no. 2, p. 180, Jan. 2018.

[26] S. Wang et al., "Trophic state assessment of global inland waters using a MODIS-derived Forel–Ule index," *Remote Sens. Environ.*, vol. 217, pp. 444–460, Nov. 2018.

[27] J. Pitarch, M. Bellacicco, S. Marullo, and H. J. van der Woerd, "Global maps of Forel–Ule index, hue angle and secchi disk depth derived from 21 years of monthly ESA ocean colour climate change initiative data," *Earth Syst. Sci. Data*, vol. 13, no. 2, pp. 481–490, Feb. 2021.

[28] M. Ye and Y. Sun, "Review of the Forel-Ule index based on in situ and remote sensing methods and application in water quality assessment," *Environ. Sci. Pollut. Res.*, vol. 29, no. 9, pp. 13024–13041, Feb. 2022.

[29] A. A. Gitelson et al., "Relationship between gross primary production and chlorophyll content in crops: Implications for the synoptic monitoring of vegetation productivity," *J. Geophys. Res.*, vol. 111, 2006, Art. no. D08S11.

[30] D. Rundquist, R. Perk, B. Leavitt, G. Keydan, and A. Gitelson, "Collecting spectral data over cropland vegetation using machine-positioning versus hand-positioning of the sensor," *Comput. Electron. Agricult.*, vol. 43, no. 2, pp. 173–178, May 2004.

Authorized licensed use limited to: Aerospace Information Research Institute. Downloaded on October 19,2023 at 00:37:32 UTC from IEEE Xplore. Restrictions apply.

[31] A. Viña, "Satellite monitoring of vegetation dynamics: Sensitivity enhancement by the wide dynamic range vegetation index," *Geophys. Res. Lett.*, vol. 31, no. 4, pp. 373–394, 2004.

[32] A. A. Gitelson, "Remote estimation of canopy chlorophyll content in crops," *Geophys. Res. Lett.*, vol. 32, no. 8, 2005, Art. no. L08403.

[33] A. L. Nguy-Robertson and A. A. Gitelson, "Algorithms for estimating green leaf area index in C3 and C4 crops for MODIS, Landsat TM/ETM+, MERIS, sentinel MSI/OLCI, and venμs sensors," *Remote Sens. Lett.*, vol. 6, no. 5, pp. 360–369, Apr. 2015.

[34] Q. Sun, Q. Jiao, X. Qian, L. Liu, X. Liu, and H. Dai, "Improving the retrieval of crop canopy chlorophyll content using vegetation index combinations," *Remote Sens.*, vol. 13, no. 3, p. 470, Jan. 2021.

[35] M. Xu et al., "Retrieving leaf chlorophyll content using a matrix-based vegetation index combination approach," *Remote Sens. Environ.*, vol. 224, pp. 60–73, Apr. 2019.

[36] D. Djudd and G. Vishecky, *Color in Business, Science and Industry*. New York, NY, USA: Wiley, 1975.

[37] W. H. Venable, "Accurate tristimulus values from spectral data," *Color Res. Appl.*, vol. 14, no. 5, pp. 260–267, Oct. 1989.

[38] G. Wyszecki and V. S. Stiles, *Color Science: Concepts and Methods, Quantitative Data and Formulas*. New York, NY, USA: Wiley, 1967.

[39] R. P. Bukata, D. V. Pozdnyakov, J. H. Jerome, and F.J. Tanis, "Validation of a radiometric color model applicable to optically complex water bodies," *Remote Sens. Environ.*, vol. 81, nos. 2–3, pp. 416–426, Aug. 2001.

[40] M. R. Wernand and H. J. V. D. Woerd, "Spectral analysis of the Forel–Ule ocean colour comparator scale," *J. Eur. Opt. Soc-Rapid.*, vol. 5, Apr. 2010, Art. no. 10014s.

[41] J.-B. Feret et al., "PROSPECT-4 and 5: Advances in the leaf optical properties model separating photosynthetic pigments," *Remote Sens. Environ.*, vol. 112, no. 6, pp. 3030–3043, Jun. 2008.

[42] H. Mangine, K. Jakes, and C. Noel, "A preliminary comparison of CIE color differences to textile color acceptability using average observers," *Color Res. Appl.*, vol. 30, no. 4, pp. 288–294, Aug. 2005.

[43] J. W. Rouse, R. H. Haas, J. A. Schell, and D. W. Deering, "Monitoring vegetation systems in the Great Plains with ERTS," in *Proc. 3rd ERTS-1 Symp. (NASA)*, Washington, DC, USA, Jan. 1974, pp. 309–317.

[44] J. Zhen et al., "Mapping leaf chlorophyll content of mangrove forests with Sentinel-2 images of four periods," *Int. J. Appl. Earth Observ. Geoinf.*, vol. 102, Oct. 2021, Art. no. 102387.

[45] D. Li et al., "Assessing a soil-removed semi-empirical model for estimating leaf chlorophyll content," *Remote Sens. Environ.*, vol. 282, Dec. 2022, Art. no. 113284.

[46] L. Bacci, M. De Vincenzi, B. Rapi, B. Arca, and F. Benincasa, "Two methods for the analysis of colorimetric components applied to plant stress monitoring," *Comput. Electron. Agricult.*, vol. 19, no. 2, pp. 167–186, Jan. 1998.

[47] S. P. Yadav, Y. Ibaraki, and S. Dutta Gupta, "Estimation of the chlorophyll content of micropropagated potato plants using RGB based image analysis," *Plant Cell, Tissue Organ Culture (PCTOC)*, vol. 100, no. 2, pp. 183–188, Feb. 2010.

[48] F. Vesali, M. Omid, A. Kaleita, and H. Mobli, "Development of an Android app to estimate chlorophyll content of corn leaves based on contact imaging," *Comput. Electron. Agricult.*, vol. 116, pp. 211–220, Aug. 2015.

[49] P. J. Mohan and S. D. Gupta, "Intelligent image analysis for retrieval of leaf chlorophyll content of Rice from digital images of smartphone under natural light," *Photosynthetica*, vol. 57, no. 2, pp. 388–398, May 2019.

[50] C. Connolly and T. Fleiss, "A study of efficiency and accuracy in the transformation from RGB to CIELAB color space," *IEEE Trans. Image Process.*, vol. 6, no. 7, pp. 1046–1048, Jul. 1997.

[51] L. Luo, K. M. Tsang, H.-L. Shen, S.-J. Shao, and J. H. Xin, "An investigation of how the texture surface of a fabric influences its instrumental color," *Color Res. Appl.*, vol. 40, no. 5, pp. 472–482, Oct. 2015.

[52] P. Lou et al., "An effective method for canopy chlorophyll content estimation of Marsh vegetation based on multiscale remote sensing data," *IEEE J. Sel. Topics Appl. Earth Observ. Remote Sens.*, vol. 14, pp. 5311–5325, May 2021.

[53] C. Liu, H. Li, A. Su, S. Chen, and W. Li, "Identification and grading of maize drought on RGB images of UAV based on improved U-Net," *IEEE Geosci. Remote Sens. Lett.*, vol. 18, no. 2, pp. 198–202, Feb. 2021.

[54] H. Croft et al., "The global distribution of leaf chlorophyll content," *Remote Sens. Environ.*, vol. 236, Jan. 2020, Art. no. 111479.

[55] M. Xu et al., "Retrieving global leaf chlorophyll content from MERIS data using a neural network method," *ISPRS J. Photogramm. Remote Sens.*, vol. 192, pp. 66–82, Oct. 2022.

[56] E. Boegh et al., "Remote sensing of LAI, chlorophyll and leaf nitrogen pools of crop and grasslands in five European landscapes," *Biogeosci. Discuss.*, vol. 9, no. 8, pp. 10149–10205, Aug. 2012.

[57] R. Houborg and M. F. McCabe, "A hybrid training approach for leaf area index estimation via cubist and random forests machine-learning," *ISPRS J. Photogramm. Remote Sens.*, vol. 135, pp. 173–188, Jan. 2018.

[58] T. K. Gill and S. R. Phinn, "Improvements to ASTER-derived fractional estimates of bare ground in a savanna rangeland," *IEEE Trans. Geosci. Remote Sens.*, vol. 47, no. 2, pp. 662–670, Feb. 2009.

[59] Q. Jiao, B. Zhang, J. Liu, and L. Liu, "A novel two-step method for winter wheat-leaf chlorophyll content estimation using a hyperspectral vegetation index," *Int. J. Remote Sens.*, vol. 35, no. 21, pp. 7363–7375, Nov. 2014.

[60] Y. Li and S. Liang, "Evaluation of reflectance and canopy scattering coefficient based vegetation indices to reduce the impacts of canopy structure and soil in estimating leaf and canopy chlorophyll contents," *IEEE Trans. Geosci. Remote Sens.*, vol. 61, 2023, Art. no. 4403015.

[61] A. Muhuri et al., "Performance assessment of optical satellite-based operational snow cover monitoring algorithms in forested landscapes," *IEEE J. Sel. Topics Appl. Earth Observ. Remote Sens.*, vol. 14, pp. 7159–7178, 2021.

[62] P. P. J. Roosjen, B. Brede, J. M. Suomalainen, H. M. Bartholomeus, L. Kooistra, and J. G. P. W. Clevers, "Improved estimation of leaf area index and leaf chlorophyll content of a potato crop using multi-angle spectral data—Potential of unmanned aerial vehicle imagery," *Int. J. Appl. Earth Observ. Geoinf.*, vol. 66, pp. 14–26, Apr. 2018.

[63] D. Li et al., "Improved estimation of leaf chlorophyll content of row crops from canopy reflectance spectra through minimizing canopy structural effects and optimizing off-noon observation time," *Remote Sens. Environ.*, vol. 248, Oct. 2020, Art. no. 111985.

[64] T. Miura, A. R. Huete, H. Yoshioka, and B. N. Holben, "An error and sensitivity analysis of atmospheric resistant vegetation indices derived from dark target-based atmospheric correction," *Remote Sens. Environ.*, vol. 78, no. 3, pp. 284–298, Dec. 2001.

[65] F. Daumard, Y. Goulas, A. Ounis, R. Pedrós, and I. Moya, "Measurement and correction of atmospheric effects at different altitudes for remote sensing of sun-induced fluorescence in oxygen absorption bands," *IEEE Trans. Geosci. Remote Sens.*, vol. 53, no. 9, pp. 5180–5196, Sep. 2015.

[66] H. Liu et al., "Evaluation of ocean color atmospheric correction methods for Sentinel-3 OLCI using global automatic in situ observations," *IEEE Trans. Geosci. Remote Sens.*, vol. 60, 2022, Art. no. 4206319.

[67] E. F. Vermote, D. Tanre, J. L. Deuze, M. Herman, and J.-J. Morcette, "Second simulation of the satellite signal in the solar spectrum, 6S: An overview," *IEEE Trans. Geosci. Remote Sens.*, vol. 35, no. 3, pp. 675–686, May 1997.

[68] R. Fensholt, I. Sandholt, and S. Stisen, "Evaluating MODIS, MERIS, and VEGETATION vegetation indices using in situ measurements in a semiarid environment," *IEEE Trans. Geosci. Remote Sens.*, vol. 44, no. 7, pp. 1774–1786, Jul. 2006.

[69] L. Dufor?t, R. Frouin, and P. Dubuisson, "Importance and estimation of aerosol vertical structure in satellite ocean-color remote sensing," *Appl. Opt.*, vol. 46, no. 7, pp. 1107–1119, Mar. 2007.

[70] Q. Vanhellemont, "Sensitivity analysis of the dark spectrum fitting atmospheric correction for metre- and decametre-scale satellite imagery using autonomous hyperspectral radiometry," *Opt. Exp.*, vol. 28, no. 20, pp. 29948–29965, Sep. 2020.

[71] N. Delavarpour, C. Koparan, J. Nowatzki, S. Bajwa, and X. Sun, "A technical study on UAV characteristics for precision agriculture applications and associated practical challenges," *Remote Sens.*, vol. 13, no. 6, p. 1204, Mar. 2021.

[72] J. Yang, L. Xiao, Y.-Q. Zhao, and J. C. Chan, "Variational regularization network with attentive deep prior for hyperspectral–multispectral image fusion," *IEEE Trans. Geosci. Remote Sens.*, vol. 60, 2022, Art. no. 5508817.

[73] W. J. D. van Leeuwen, B. J. Orr, S. E. Marsh, and S. M. Herrmann, "Multi-sensor NDVI data continuity: Uncertainties and implications for vegetation monitoring applications," *Remote Sens. Environ.*, vol. 100, no. 1, pp. 67–81, Jan. 2006.

[74] X. Fan and Y. Liu, "Multisensor normalized difference vegetation index intercalibration: A comprehensive overview of the causes of and solutions for multisensor differences," *IEEE Geosci. Remote Sens. Mag.*, vol. 6, no. 4, pp. 23–45, Dec. 2018.

Authorized licensed use limited to: Aerospace Information Research Institute. Downloaded on October 19,2023 at 00:37:32 UTC from IEEE Xplore. Restrictions apply.



Quanjun Jiao received the B.S. degree in geographic information system from Peking University, Beijing, China, in 2003, and the Ph.D. degree in cartography and geographic information system from the Institute of Remote Sensing Applications, Chinese Academy of Sciences (CAS), Beijing, in 2008.

He is currently an Associate Professor with the Aerospace Information Research Institute, CAS. His research interests include retrieval of vegetation biophysical and biochemical parameters, and application of remote sensing in vegetation monitoring at regional and global scales.



Bing Zhang (Fellow, IEEE) received the B.S. degree in geography from Peking University, Beijing, China, in 1991, and the M.S. and Ph.D. degrees in remote sensing from the Institute of Remote Sensing Applications, Chinese Academy of Sciences (CAS), Beijing, in 1994 and 2003, respectively.

He is currently a Full Professor and the Deputy Director of the Aerospace Information Research Institute, CAS. His research interests include the development of mathematical and physical models and image processing software for the analysis of hyperspectral remote sensing data in many different areas. He has been serving as a Technical Committee Member for the IEEE Workshop on Hyperspectral Image and Signal Processing since 2011, the President for the Hyperspectral Remote Sensing Committee of the China National Committee of the International Society for Digital Earth since 2012, and the Standing Director for the Chinese Society of Space Research (CSSR) since 2016. He is the Student Paper Competition Committee Member of IGARSS from 2015 to 2019.

Dr. Zhang received the National Science Foundation for Distinguished Young Scholars of China in 2013 and the 2016 Outstanding Science and Technology Achievement Prize of the Chinese Academy of Sciences, the highest level of awards for CAS scholars. His creative achievements were rewarded with ten important prizes from the Chinese government and special government allowances from the Chinese State Council. He has been serving as an Associate Editor for IEEE TRANSACTIONS ON GEOSCIENCE AND REMOTE SENSING (TGRS).



Wenjiang Huang received the Ph.D. degree in cartography and geographic information system from Beijing Normal University, Beijing, China, in 2005.

He is currently a Professor with the Aerospace Information Research Institute, Chinese Academy of Sciences (CAS), Beijing. His research interests include quantitative remote sensing research and application in vegetation.



Huichun Ye received the Ph.D. degree in soil science from China Agricultural University, Beijing, China, in 2014.

He is currently an Associate Professor with the Aerospace Information Research Institute, Chinese Academy of Sciences (CAS), Beijing. His research interests include quantitative remote sensing application in vegetation monitoring and precision agriculture.



Zhaoming Zhang received the B.S. degree in geographic information system from Henan University, Kaifeng, China, in 2003, the M.Sc. degree in satellite image processing from the China Remote Sensing Satellite Ground Station, Chinese Academy of Sciences (CAS), Beijing, China, in 2006, and the Ph.D. degree in cartography and geographic information system from the Institute of Remote Sensing Applications, CAS, Beijing, in 2009.

He is a Professor with the Aerospace Information Research Institute, CAS. His research interests include information extraction from satellite image and remote sensing application.



Binxiang Qian received the B.S. degree in electrical engineering from Southwest Jiaotong University, Chengdu, China, in 2020. He is currently pursuing the Ph.D. degree in cartography and geographic information system with the Key Laboratory of Digital Earth Science, Aerospace Information Research Institute, Chinese Academy of Sciences (CAS), Beijing, China.

His research interests include hyperspectral LiDAR, radiative transfer model, hyperspectral remote sensing, 3-D/4-D structure modeling of crops, and monitoring the vertical distribution of canopy chlorophyll content.



Bohai Hu received the B.S. degree in agricultural resources and environment from Sichuan Agricultural University, Chengdu, China, in 2022. He is currently pursuing the Ph.D. degree in cartography and geographic information system with the Key Laboratory of Digital Earth Science, Aerospace Information Research Institute, Chinese Academy of Sciences (CAS), Beijing, China.

His research interest is remote sensing of vegetation carbon sink.



Shenglei Wang received the Ph.D. degree in cartography and geographic information system from the University of Chinese Academy of Sciences, Beijing, China, in 2018.

From 2017 to 2019, she was a Joint-Training Ph.D. Student and then a Research Fellow at the Department of Biological and Environmental Science, University of Stirling, Stirling, U.K. From 2019 to 2020, she was a Boya Post-Doctoral Research Fellow at Peking University, Beijing. She is currently an Associate Professor with the Aerospace Information Research Institute, Chinese Academy of Sciences (CAS), Beijing. Her research interests include water color remote sensing, bio-optical properties, and water quality modeling in regional and global optically complex waters.

Authorized licensed use limited to: Aerospace Information Research Institute. Downloaded on October 19,2023 at 00:37:32 UTC from IEEE Xplore. Restrictions apply.